CHALMERS

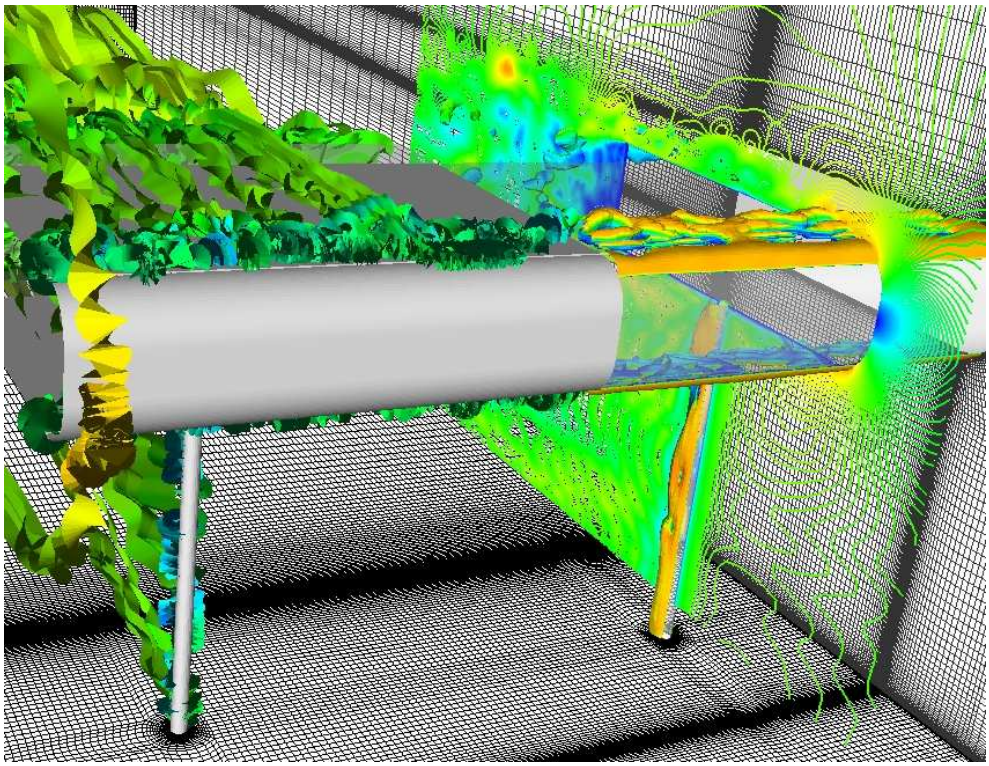

Large-Eddy Simulations of the Flow around a Vehicle Model with Active Drag Control

JOÃO FERNANDES

Department of Applied Mechanics

Chalmers University of Technology

Göteborg, Sweden, 2007

MASTER'S THESIS 2007:66

Thesis for the degree of Master of Science

in

Automotive Engineering

Large-Eddy Simulations of the Flow around a Vehicle Model with Active Drag Control

João Fernandes

Division of Fluid Dynamics
Department of Applied Mechanics
Chalmers University of Technology
Göteborg, Sweden, 2007

Large-Eddy Simulations of the Flow around a Vehicle Model with Active Drag Control
João Fernandes

Thesis for the Degree of Master of Science in Automotive Engineering

Master's Thesis 2007:66
ISSN 1652-8557
Department of Applied Mechanics
Division of Fluid Dynamics
Chalmers University of Technology
SE-412 96 Göteborg
Sweden
Telephone: +46 (0)31-7721400

Cover Page:
The flow around the vehicle model mounted in the wind tunnel. Instantaneous coherent structures are visualized from a pressure isosurface, at the right half. Instantaneous velocity contours are shown in a domain plane. Streamlines are created from instantaneous vortex cores and are visualized in the left half of the domain using ribbons.

Department of Applied mechanics
Göteborg, Sweden 2007

The kids need education
And the streets are never clean
I've seen a certain disposition, prevailing in the wind,
Sweet change if anybody's listening?
Emergency on Planet Earth
Is that life that I am witnessing
Or just another wasted birth.

Jason Cheetham

Large-Eddy Simulations of the Flow around a Vehicle Model with Active Drag Control

by

João Fernandes
joaof@student.chalmers.se
Department of Applied Mechanics
Division of Fluid Dynamics
Chalmers University of Technology
SE-412 96 Gteborg, Sweden

Abstract

The ability of actively controlling the flow around a simplified vehicle in order to achieve drag reduction is investigated. LES is recognized as a tool capable of providing the accurate temporal description of the transient nature of the flow around bluff bodies. It is thus selected to understand the deviation from the natural case of the instantaneous and time-averaged controlled flow around a two-dimensional Ahmed body with 0° slant angle mounted in a wind tunnel. A low Reynolds number flow is selected as an initial case-study in order to understand the effects of harmonic wake actuation on the drag force response. The influence of the actuation parameters is investigated at $Re_h = 2 \times 10^3$, namely actuation slot location, actuation frequency and actuation amplitude. It is found that the alternating sequence of strong vortex formation, characteristic of the natural flow, is suppressed by harmonic actuation on the flow's wake and that this is the main mechanism responsible for drag reduction. Two synchronized vortices of similar amplitude are found both in the instantaneous and time-averaged controlled flow topology and these are responsible for a considerable pressure recovery in the wake region, leading to a drag reduction of 2.5% at this Reynolds number. The previous research also proves that a far more uniform pressure distribution on the wake can be attained in the instantaneous controlled flow, particularly at peak suction instants.

The understanding gained here about the underlying physical problem is subsequently applied to obtain a controlled flow at $Re_h = 2 \times 10^4$. The efficiency of the control strategy is demonstrated by a drag force signal that follows the actuation frequency, with maximum and minimum drag force found respectively at peak blowing and peak suction instants. Finally, the potential for beneficial performance increase in vehicle aerodynamics through active flow control is proved by a drag reduction of 10% achieved at this Reynolds number.

Key words: LES, Drag Reduction, Active Flow Control.

Acknowledgments

This thesis represents the final work leading to the Master of Science degree in Automotive Engineering, and took place in Chalmers University of Technology, Gothenburg, Sweden. I dedicate it to my family, who always made it possible for me to enlarge my education and my vision of the world, Maria Odete Ventura and Dionísio Fernandes.

I would like to acknowledge my supervisor, Dr. Siniša Krajnović, for all of his teaching, scientific guidance and encouragement throughout the course of this project. Our discussions were always valuable moments to me, giving me insight and pushing me further in my research.

I would like to express my recognition to Mohamad El-Alti and Hassan Hemida, for their time and disposition to answer my questions and for their help fixing and solving practical problems. Thank you, Fluid Dynamics Division, for the daily efforts to make the people who work there welcome and comfortable.

The support given to this project both by CD-adapco and UNICC is also recognized. Computer time on ADA supercomputer provided by UNICC at Chalmers is gratefully acknowledged.

I would like to mention the availability by Dr. Lars Henning and the Measurement and Control Group from Berlin University of Technology in providing the experimental data, publications and informations from their work in Active Flow Control. This is gratefully acknowledged.

I also would like to thank Pedro Valente, for challenging me to study the mysteries of Turbulence. This allowed me to discover new interesting scientific problems and to greatly extend my undergraduate background.

Finally, to Catarina Baptista, for all your love and support throughout the last few years, thank you.

João Fernandes.

Nomenclature

Abbreviations

AFC	Active Flow Control
CFD	Computational fluid dynamics
CFL	Courant-Friedrichs-Levy
DES	Detached-Eddy Simulation
LES	Large-Eddy Simulation
PIV	Particle Image Velocimetry
POD	Proper-Orthogonal Decomposition
URANS	Unsteady Reynolds Averaged Navier-Stokes

Lower-case Greek

ν	Kinematic viscosity
ν_{SGS}	Subgrid kinematic viscosity
ω_A	Actuation frequency
ϕ	Actuation angle
ρ	Density
τ_{ij}	Subgrid stress tensor
$\tilde{\varepsilon}$	Kinetic energy rate through cut-off
ε	Kinetic energy dissipation rate
ε_I	Injection of kinetic energy rate trough the cut-off

Upper-case Greek

Δt	Time step
Δ	LES filter characteristic length

Lower-case Roman

$\overline{u}$	Resolved instantaneous velocity
$\vec{x}$	Position vector, (x,y,z) in Cartesian coordinate system
f	Frequency
k	Wave Number

p	Pressure
t	Time
t^*	Dimensionless time unit
u	Instantaneous velocity
u_i	Cartesian components of the instantaneous velocity vector
u_A	Actuation velocity
x, y, z	Cartesian coordinate vector components
Subscripts	
∞	Free-stream conditions
SGS	Subgrid scale
Superscripts	
$-$	Spatially filtered quantity
Upper-case Roman	
$\overline{S}_{ij}$	Resolved instantaneous strain-rate tensor
C_d	Drag force coefficient
C_l	Lift force coefficient
C_p	Pressure coefficient
C_S	Smagorinsky model constant
C_μ	Actuation dimensionless momentum coefficient
E	Energy Spectrum
F_d	Drag force
F_l	Lift force
H	Model's height
L	Model's length
Re	Reynolds Number
St	Strouhal Number
W	Model's width

Contents

Abstract **v**

Acknowledgments **vii**

Nomenclature **ix**

1 The active flow control problem **1**
1.1 Introduction 1
1.2 Active control of the flow around bluff bodies 3

2 About the level of approximation and the governing equations **5**
2.1 Scale Separation 5
2.2 Governing equations 7

3 Correlating AFC parameters with drag reduction **11**
3.1 Introduction 11
3.2 Vehicle model and computational domain 11
3.3 Boundary conditions 14
3.4 Resolution, SGS modeling and numerical details 14
3.5 Slot location 17
3.6 Actuation amplitude and frequency 19
3.7 The instantaneous and time-averaged flows 21

4 Making LES of the flow around a simplified vehicle with active control **33**
4.1 Geometry, boundary conditions and resolution 33
4.2 Drag control results 36
4.3 Exploring the flow 39

5 Conclusions and suggestions for future work **49**

Bibliography **53**

Chapter 1

The active flow control problem

The main issues about the active flow control problem are discussed. The past experimental and computational research in active flow control is reviewed. Different methodologies are presented. My personal view of the questions needed to be answered and overcome in the field of numerical simulation of active flow control is given to consideration. In section 1.2, special attention is given to recent research on the control of the flow around bluff bodies since that is the main goal of this investigation.

1.1 Introduction

Active flow-control is a part of a vast multi-disciplinary field known as Flow Control. Following the concept by Gad-el-Hak, M.et al. [1], flow control can be defined as the methodology that allows bringing the flow from an initial state to a desired state where some of its features are enhanced, reduced or simply modified. Controlling the flow features has been a research goal as old as the research on flows themselves, since the need to control separation, mixing, drag or lift, large vortical structures or noise as always been present in an uncountable number of flows.

It is only recently that the progresses in control systems, electronics, actuators, sensors and computational techniques enables the utilization of tools that can cope with the non-linearity of the fluid's physics and still give an affordable description of flows of engineering interest. The technology has provided a mean of utilizing unsteady and fast-responding control methods that can be integrated into the flow control research. An extensive literature survey in the research that has been performed in active flow control is provided both in [1] and Collins et al. [2].

Current state of the art research methodologies used in flow control investigation are summarized here. A research through the work in boundary layer control shows that very different approaches have been attempted in the domain of open and closed-loop control. The opposition control strategy[1]is described in [3] and has been applied in the control of streamwise vortices and streaks in boundary layers by Stuart and Reynolds [4]. Among others authors, Rathnasingham and Breuer [5] and Yong and Gaster [6], have used the classical control theory approach to the boundary layer control problem. Active

[1]The simplest type of feedback control, where the selection of the measured quantity and the control mechanism relies on the understanding of the underlying physics of the problem.

control of the flow around bluff bodies has been initiated with the work on reference flows such as the cylinder flow. Experimental investigations in the manipulation of the cylinder near wake, through rotational forcing and jet-slot actuation, have accomplished vortex shedding delay and cylinder loading decrease and have been a research topic until today, Fu and Rockwell [7]. A mathematical approach to the same problem has been pursued by Gillies[8] making use of the power of the Proper-Orthogonal Decomposition to extract the relevant set of POD modes of the cylinder wake which then allowed the design of a closed-loop control algorithm to manipulate these large-wake turbulent structures. A method based on the construction of low-dimensional Galerkin Models has also been proposed by Gerhard et al. [9] in order to suppress the vortex shedding downstream a circular cylinder.

CFD methods have also been applied for many years to the active flow problem, particularly, to airfoils. Lift enhancement was achieved in the simulations by Donovan et al. [10] and optimization studies have been performed subsequently, for example, by Ekaterinaris [11], Duvigneau and Visonneau [12], Schatz et al. [13]. These are focused on oscillatory forcing and have used URANS with eddy-viscosity closure models as their main tool. Drag reduction and lift control of a stalled airfoil has been successfully accomplished in the semi-implicit finite element based LES performed by Kjellgren [14]. Spalart et al. [15] has also aimed to simulate periodic excitation on the flap of a stalled airfoil, but using DES. The results have shown, however, poor agreement with the wind tunnel experimental data.

The former investigations have shown that there are a number of unresolved issues in CFD arising from active flow control implementation. Firstly, the introduction of unsteady control in aerodynamic design challenges the researcher to model the actuator and the actuator-induced flow. This has been performed in [11], [12], [15] through the implementation of simplified boundary conditions on the geometry of the airfoil. Oscillatory actuation is then modelled as unsteady suction and blowing through the wall using a simple analytic function, a harmonic function so that an equal amount of mass is injected by blowing and extracted by suction and no net flux is added. Clearly, the main problem here is to ensure that the profile in the cells adjacent to the actuator follows the exact profile determined by the harmonic function. A different approach has been pursuited in the LES by You and Moin [16], where the geometry of a synthetic jet actuator has been recreated in detail in order to accurately attain the effects of the actuator-induced flow on the airfoil. Here, the velocity boundary condition is applied at the walls of the jet cavity and not on the airfoil itself. An alternative approach to both these ideas would be to couple a structural finite-element model of the actuator to the CFD code or fluid model [2]. The increasing level of complexity sustained in the three methodologies pointed out previously is, therefore, obvious. A second question in computing the flow with AFC implementation is the spatial and time resolutions in the near-actuator region. There is still no reference study of the actuator region spatial resolution's influence on the global CFD solution. Predicting the grid resolution to accurately model the AFC effect is difficult and thus, very different solutions have been found throughout the previous work. The time resolution also becomes a major issue in AFC problems, specially when concerning the implementation of zero mass flux oscillatory actuators. Unsteady actuation presupposes time-resolution in the numerical schemes and the validity of the CFD models to describe the actuator-induced flow must be questioned, [15]. Resolving the strategic

region surrounding the actuator with RANS based methodologies (either with URANS or DES) can only correctly predict the dynamics of the induced flow if the dominating flow feature is the introduced instability mechanism. However, if the incoming or the actuator generated turbulence is main mechanism responsible for the turbulent boundary layer or large scale dynamics control, then RANS methods are not expected to give the truthful transient flow description, at least without the need to adjust the modeling parameters for the new turbulence features.

A lot has been done in the field of active flow control, as the previous paragraphs illustrate. Though the progresses look promising, some steps to the general implementation of these methods in flows with real application are still missing.

1.2 Active control of the flow around bluff bodies

The active control of the flow around a generic bluff body has been the object of interest of research works, due to the economic and environmental gains in reducing the aerodynamic drag of this type of body. Statistics between 2000 and 2004 [17] reveal that 1% reduction in fuel consumption *only in* the United States truck and bus industry, would mean at the present cost of fuel a saving of about 100 million dollars and 240 thousand tons of $C0_2$ emissions per year.

Due to its greater simplicity but still its resemblance to a generic bus or truck shape, the active control of the flow around a 2-dimensional bluff body has been performed. Henning et al. [18] used open loop control and feedback control to the bluff body wake to reduce the aerodynamic drag of the body. Their experimental work consisted of harmonic actuation in time applied through two spanwise slots mounted in the elongated bluff body upper and lower trailing edges, with an angle of 45° relatively to the streamwise direction. The control mechanism on the wake was investigated for a range of actuation amplitudes and frequencies in the spectrum of Reynolds number based on the body's height of 2×10^4-6×10^4. This investigation achieved a maximum pressure recovery at $St_A = 0.17$ [2] , yielding a drag reduction of the order of 15% when both actuators are in-phase.

A different approach is suggested by Kim et al. [19] also through their work in drag reduction on a 2-D model vehicle. Here, the actuation method is a harmonic forcing (blowing and suction) in the spanwise direction of the body (at the upper and lower trailing edges) and constant in time. LES at $Re_h = 4.2\times10^3$ and experiments at $Re_h = 2\times10^4$ and $Re_h = 4\times10^4$ achieved a pressure recovery of about 30%, 36% and 18%, respectively, and demonstrated how distributed forcing can be used to change the vortical structures in the wake from nominally two to three-dimensional, thus accomplishing a pressure recovery. No aerodynamic drag data of the body is provided, though.

Active drag control of a 3-dimensional Ahmed body has been attempted in Brunn et al. [20] where experimental and numerical research is performed at $Re_h = 5\times10^5$. In this publication, experiments with periodic excitation and experiments and LES with constant blowing are presented for the slant angles of 35^o and 25^o, respectively, but yielding no more than 2.5% drag reduction. It is not yet clear from [20] if it is its early stage or it is its control strategy that is giving the poor results.

[2] Here, the Strouhal number is defined based on the actuation frequency of the actuators.

Chapter 2

About the level of approximation and the governing equations

This chapter presents the main theoretical assumptions and the governing equations behind the Large-Eddy Simulation method.

2.1 Scale Separation

The Large-Eddy Simulation method is based on the idea of separation between the large and the small scales of motion in a fully developed turbulent flow. This idea follows the work of Kolomogorov [21] and has been the most used one for a long time.

From our physical reasoning of observing a great number of flows around us, one might anticipate that the velocity fluctuations on a three-dimensional velocity field are dispersed over all the wavelengths characteristic of the flow, from the smaller scales where viscosity dominates the dissipation of the fluid's motion into heat, to the bigger scales, of the size of the system and containing most of the kinetic energy in it. It is somehow this picture we can imagine walking by a windy Autumn day and watching the very different motion of tree leaves inside a swirling vortex, some dragged at very high speed and some floating slowly in an unbalanced motion.

The question is then how can we separate these two scales of motion and, more importantly, why. Kolmogorov showed that for *homogeneous* [1] and *isotropic*[2] turbulence in flows *at very high Reynolds number* there exists a total separation between the energy containing scales and the dissipative scales of turbulent motion. Under these conditions, Kolmogorov's idea is that the turbulence in the intermediate scales, nominated as the *inertial subrange*, is independent of initial and boundary conditions. The turbulence scales in the inertial range are said to be in *local equilibrium* and do not retain any memory of the effects of the anisotropy of the larger scales on them. This is known to be Kolomogorov's hypothesis of *universal statistics* and *self-similarity* of turbulence in the inertial subrange. The second similarity hypothesis states that within the inertial subrange the nature of turbulence is independent of the fluid's viscosity.

[1] Defined as the invariance of the flow statistics to translation.

[2] Defined as the invariance of the flow statistics to rotation and reflection.

According to these hypothesis, the energy spectrum in the inertial subrange, $E(k)$, can be derived using dimensional analysis: it must only be a function of the kinetic energy dissipation rate, ε, and the wave number, k,

$$E(k) = f(\varepsilon, k) \tag{2.1}$$

from which the famous $-5/3$ *law* for the Energy Spectrum in the inertial subrange is deduced as,

$$E(k) = C\varepsilon^{2/3}k^{-5/3} \tag{2.2}$$

where C is named as the Kolmogorov constant.

Undoutably simple and yet, powerful, the $-5/3$ law draws the physical picture of a cascade process: the kinetic energy of the large turbulent motions is consecutively transferred to the scales of motions of increasing wavenumber, until the viscosity takes over and dissipates it into heat. Another assumption of this picture is that the forward energy cascade process occurs, mainly, due to the interaction of wavenumbers of comparable magnitude.

However, though in use for quite a long time, this picture is far from bringing the final answer to the mystery of turbulence. Recently, Gamard and George [22] have used a Near-Assymptotics analysis of the turbulent energy spectrum and constructed two scaled profiles that could describe the entire spectrum for finite values of Reynolds number. They have shown that in the overlap region, the spectra follow a power law $E(k) = Ck^{-5/3+\mu}$ where μ and C are Reynolds number dependent and that only in the limit of infinite Reynolds number $\mu \to 0$ and $C \to constant$, that is, Kolmogorov's theory is only recovered in the limit. Other research, both theoretical and computational, demonstrated that the energy transfer in the inertial subrange was composed of a forward and an inverse transfer component. This seems not to correspond to the Kolmogorov's energy cascade image since the intermediate scales of motion seem to play also a role in the dynamics of the large scales.

Why is this important to the LES method? Because it would be impossible with today's computers to try to describe all the scales of motion for flows at high Reynolds number. Therefore, the theorical analysis of *fully developed isotropic homogeneous turbulence* provides a concept of scale separation that can be used to, on one hand, accurately compute the large scales of motion and inter-scale interactions, and on the other hand, develop models to include the scales which are too small to be computed. As the next section will point out, this is achieved in LES through a band-pass filter which is *assumed* to be placed within the inertial subrange.

Nevertheless, one must bear in mind the limitations of the theory behind the method:

1. The local turbulence isotropy hypothesis is only valid in the limit of infinite Reynolds number and, consequently, is not applicable to real flows.

2. The cascade energy process may not be a cascade: backscatter does occur.

3. Direct interactions between the large and small scales can exit in real flows at intermediate Reynolds number: only at infinite Reynolds number we can speak about a complete scale separation.

2.2 Governing equations

The scale separation the LES method is based on is the separation between the large and small scales, which then are defined relatively to a cut-off length. In physical space, the scales with characteristic size greater than the cut-off length are named as *resolved scales* and those smaller are called *subgrid scales*. The same can be said in Fourier space, being the resolved scales those with wavenumber smaller than the cut-off wave number and the subgrid scales those with greater one. The cut-off represents, therefore, a scale high-pass filter, that is, low-pass in frequency.

The filtering is mathematically defined in physical space as a convolution product. The *resolved* part, $\overline{u}(\vec{x},t)$, of the *exact* velocity field, $u(\vec{x},t)$, is defined formally as:

$$\overline{u}(\vec{x},t) = \int_{-\infty}^{+\infty}\int_{-\infty}^{+\infty} u(\vec{\xi},t')G(\vec{x}-\vec{\xi},t-t')dt'd^3\vec{\xi} \tag{2.3}$$

in which the convolution kernel G is a characteristic of the filter used, i.e., the cut-off characteristic length, Δ.

One of the classical filters and one of the most used in LES is the box or top-hat filter, which can be defined, for a mono-dimensional case, as:

$$G(x-\xi) = \begin{cases} \frac{1}{\Delta} & \text{if } |x-\xi| \leq \frac{\Delta}{2} \\ 0 & \text{otherwise} \end{cases} \tag{2.4}$$

or, using the definition of the Heaviside function, as:

$$G = \frac{1}{\Delta}H(\frac{\Delta}{2} - |x-\xi|) \tag{2.5}$$

The application of the filtering operation to the fluid's fundamental equations, making use of the commutation and derivation properties of the filter, leads to the formulation of the governing equations for the LES method, named as the filtered Navier-Stokes equations and the filtered continuity equation[3]:

$$\frac{\partial\overline{u}_i}{\partial t} + \frac{\partial}{\partial x_j}(\overline{u_iu_j}) = -\frac{1}{\rho}\frac{\partial\overline{p}}{\partial x_i} + \nu\frac{\partial}{\partial x_j}(\frac{\partial\overline{u}_i}{\partial x_j} + \frac{\partial\overline{u}_j}{\partial x_i}) \tag{2.6}$$

$$\frac{\partial\overline{u}_i}{\partial x_i} = 0 \tag{2.7}$$

The filtered equations bring out the non-linear term $\overline{u_iu_j}$, which can not be solved directly. However, rearranging this term as:

$$\overline{u_iu_j} = (\overline{u_iu_j} - \overline{u}_i\overline{u}_j) + \overline{u}_i\overline{u}_j \tag{2.8}$$

the Navier-Sokes equations can then be rewritten as a function of the filtered velocity only:

$$\frac{\partial\overline{u}_i}{\partial t} + \frac{\partial}{\partial x_j}(\overline{u}_i\overline{u}_j) = -\frac{1}{\rho}\frac{\partial\overline{p}}{\partial x_i} + \nu\frac{\partial}{\partial x_j}(\frac{\partial\overline{u}_i}{\partial x_j} + \frac{\partial\overline{u}_j}{\partial x_i}) - \frac{\partial\tau_{ij}}{\partial x_j} \tag{2.9}$$

[3]Assuming incompressibility and isotropy of the fluid's properties.

in which the *subgrid stress tensor* τ is defined as

$$\tau_{ij} = \overline{u_i u_j} - \overline{u}_i \overline{u}_j \tag{2.10}$$

The same could be achieved decomposing the non-linear term as a function of the filtered velocity $\overline{u}$ and the velocity fluctuation u', using $u' = u - \overline{u}$, and following the known *Leonard decomposition* or triple decomposition [23].

Looking into equation (2.9), the mathematical formulation of the filtered Navier-Stokes equations already unveils the scale separation: all the small scale dynamics are grouped into a *subgrid term*, which will not be solved, but *modelled*. The complexity of the solution is then reduced by retaining only the large scales in the numerical solution process, which means reducing the number of degrees of freedom of the solution in both space and time. Because the terms containing u' are not directly solved, the information containing the small scales is, consequently, lost from the exact solution. Therefore, both the accuracy of the model for the subgrid scales *and* the resolution of the filter used will of course have a main role in the accuracy of the dynamics of the resolved scales.

A closure model is then needed to complete the mathematical formulation of the LES method [4]. The problem of subgrid modelling consists in representing the physical interactions between the fluctuation field u', represented by $\bigtriangledown \cdot \tau$, and the resolved field $\overline{u}$, which are expressed in the dynamics of the equation (2.9). One modeling strategy consists in modeling the action of the subgrid terms on the quantity $\overline{u}$ and not the tensor τ itself. This is called in [23] as *Functional Modeling* and physical means that a term with the same effect or function, but not necessarily the same structure, as a dissipative term is being introduced into the governing equation (2.9). The closure model is then expressed mathematically as:

$$\bigtriangledown \cdot \tau = F(\overline{u}) \tag{2.11}$$

Functional modeling requires no prior knowledge of the structure of the subgrid scales but does require that the nature of the interaction between scales and its effects are known. This is where Kolmogorv's theory about the *universal character* of the smallest turbulent scales and the nature of the Energy Spectrum provides a way to proceed. Following Kolmogorov's theory, described in *section* (2.1), if these scales are universal and independent of the large scales of the flow, then the action of the subgrid scales on the resolved scales may be *assumed* to be mainly an energetic action, so that the balance of energy transfer between both scale ranges is sufficient to describe the interaction. Implicit in this assumption is also the hypothesis about the isotropy of the small scales.

If it is further *assumed* that the energy transfer mechanism from the resolved scales to the subgrid scales is similar in nature to the molecular diffusion mechanism, then the forward energy cascade can be mathematically structured using a subgrid viscosity, denoted as ν_{SGS}. The models based in these hypothesis are named as *Subgrid Viscosity Models* and, following Boussinesq ideas, the model can be mathematically written as:

$$- \bigtriangledown \cdot \tau^d = \bigtriangledown \cdot (\nu_{SGS}(\bigtriangledown \overline{u} + \bigtriangledown^T \overline{u})) \tag{2.12}$$

[4] Though several modeling strategies and closure model exist in the LES method, only the formulation needed for the comprehension of the current work will be presented.

in which τ^d is the deviator tensor of τ:

$$\tau_{ij}^d = \tau_{ij} - \frac{1}{3}\tau_{kk}\delta ij \tag{2.13}$$

However, for the closure model to be complete, an evaluation of the subgrid viscosity is further required, since a new unknown to the problem was introduced by the previous hypothesis. This can be achieved using again global quantities related to the resolved scales and Kolmogorov's theory. Assuming that the cut-off, with characteristic cut-off length Δ, is located within the range that verifies Kolmogorov's spectrum corresponding to isotropic homogeneous turbulent flow, then three energy fluxes are defined: the injection of kinetic energy into the flow due to instabilities, denoted ε_I; the kinetic energy rate trough the cut-off, denoted $\tilde{\varepsilon}$;and the kinetic energy dissipation rate, ε. The subgrid viscosity models based on the resolved scales are of the generic form:

$$\nu_{SGS} = \nu_{SGS}(\Delta, \tilde{\varepsilon}) \tag{2.14}$$

Following the previous Kolmogorov's assumptions and using simple dimensional analysis, then the subgrid viscosity is such that:

$$\nu_{SGS} \propto \Delta^{\frac{4}{3}}\tilde{\varepsilon}^{\frac{1}{3}} \tag{2.15}$$

In order to evaluate the dissipation rate from the information retained in the resolved scales, a last hypothesis is taken from Kolmogorov's theory: *the Local Equilibrium Hypothesis*. In fact, if the subgrid scales are locally in constant spectral equilibrium, then the shape of the energy spectrum is invariant with time and a balance between kinetic energy production and dissipation is retained:

$$\langle \varepsilon_I \rangle = \langle \tilde{\varepsilon} \rangle = \langle \varepsilon \rangle = \langle 2\nu_{SGS}\overline{S}_{ij}\overline{S}_{ij} \rangle \tag{2.16}$$

where $\langle\rangle$ designates statistical average and $\overline{S}_{ij}$ is the instantaneous resolved strain rate tensor, defined by:

$$\overline{S}_{ij} \equiv \frac{1}{2}(\frac{\partial \overline{u}_i}{\partial x_j} + \frac{\partial \overline{u}_j}{\partial x_i}) \tag{2.17}$$

The theory about isotropic and homogeneous turbulence is sustained on statistical averaged quantities and not in local values in the physical space and, therefore, relation (2.16) is only true on *spacial average*. Using equation (2.16) into (2.15), then an explicit expression for the subgrid viscosity is obtained:

$$\langle \nu_{SGS} \rangle = (C_S\Delta)^2 \langle 2\overline{S}_{ij}\overline{S}_{ij} \rangle^{\frac{1}{2}} \tag{2.18}$$

Smagorinsky has used this relation in the numerical implementation of a subgrid viscosity model based on the large scales that has originated the *Smagorinsky Model*. The relation is, however, used in a local form in the physical space, in order to be adaptable to the flow being computed. There is no theoretical justification to the local use of relations that are based on assumptions that are only true for the whole. This ensures that the energy transfers through the cut-off are expressed correctly on average, but not locally. This need to retain the local equilibrium relation is the reason why the constant C_S is

flow dependent and, thus, it has to be tuned for the particular flow being calculated. The Smagorinsky Model takes then the generic closure form:

$$\nu_{SGS}(\vec{x},t) = (C_S\Delta)^2(2|\overline{S}(\vec{x},t)|^2)^{\frac{1}{2}} \tag{2.19}$$

It should be also noted that the filter characteristic length Δ is computed using the local characteristic length of the grid used to solve numerically the flow, as:

$$\Delta = (\Delta_i\Delta_j\Delta_k)^{\frac{1}{3}} \tag{2.20}$$

where Δ_i, Δ_j and Δ_k are, for each of the grid cells, the corresponding cell size in each of the coordinate system principal directions.

Equations (2.9), (2.12), (2.19) and (2.20) constitute the set of governing equations needed to implement numerically the LES method, using the Smagorinsky subgrid viscosity closure model. The discretization in space and time of these equations allows to iteratively solve these governing equations and additional details on the implementation of the numerical methods can be found, for example, in Krajnović, S. [24].

Chapter 3

Correlating AFC parameters with drag reduction

The computational details of the present Large-Eddy Simulations are described. The model, the spacial and time resolutions and the boundary conditions are discussed for both the natural and controlled flow configurations. Investigation of slot location, actuation frequency and actuation amplitude influence on drag reduction is performed at $Re_h = 2 \times 10^3$. The conclusions retrieved from this study are extrapolated for the computational investigation of the controlled flow at $Re_h = 2 \times 10^4$.

3.1 Introduction

Due to the computational cost of making LES of flows at high Reynolds number, the flow around a simplified vehicle at a Reynolds number of 2×10^3, based on the free-stream velocity and the model's height, was selected to be the initial test case. Though the engineering applicableness of the results is small, this study allowed us to gain the insight about the relative influence of the parameters used in the flow control strategy. It was, thus, of great usefulness. Three main set of parameters are investigated: the slot location, the actuation frequency and the actuation amplitude, and their effects on the body forces of the controlled flow. The experimental work by Henning, L. et al. [18] is the main source for reference results and, therefore, the model's geometry is similar to that of this reference. For greater simplicity, the circular rods used in [18] to mount the model in the wind tunnel test section are excluded in the LES at $Re_h = 2 \times 10^3$.[1]

3.2 Vehicle model and computational domain

The simplified vehicle model consists of a bluff body with the generic shape of a bus and its geometry is presented in Figs. 3.1 and 3.2. The coordinate system origin used is located at center of the model's rear face, with the *xy plane* and the *xz plane* corresponding respectively to the longitudinal and vertical sections of symmetry. Streamwise, transverse

[1] As shown in section 4.1. these rods are included in the LES at $Re_h = 2 \times 10^4$, where the accuracy of the flow's description is the main purpose of the research.

and spanwise directions are therefore associated with the *x, y and z* axis, respectively. As in [18], the model has the same spanwise length as the computational domain, $W = B = 0.55m$, and thus, it is a 2-Dimensional body. The model's height and length are, respectively, $H = 0.072m$ and $L = 0.262m$, and the fillet radius on the front face is $R = 0.025m$. The trip tape at the upper and lower faces used in the experimental work is included in the geometry through the step with dimensions $d_1 = 0.0008m$ and $d_2 = 0.005m$.

The model is vertically centered in a computational domain of $C = 7.7H$. The distance from the model surfaces to the inflow and outflow planes must be long enough to avoid the influence of the model on the total pressure there and following the work by Krajnović and Davidson [25], [26], the computational domain is extended $X_1 = 10.25H$ upstream and $X_2 = 20.83H$ downstream the body, as shown in Fig. 3.2. Beside verifying the usual computational requeriments, these lengths were also chosen to match the dimensions of the wind tunnel test section in [18].

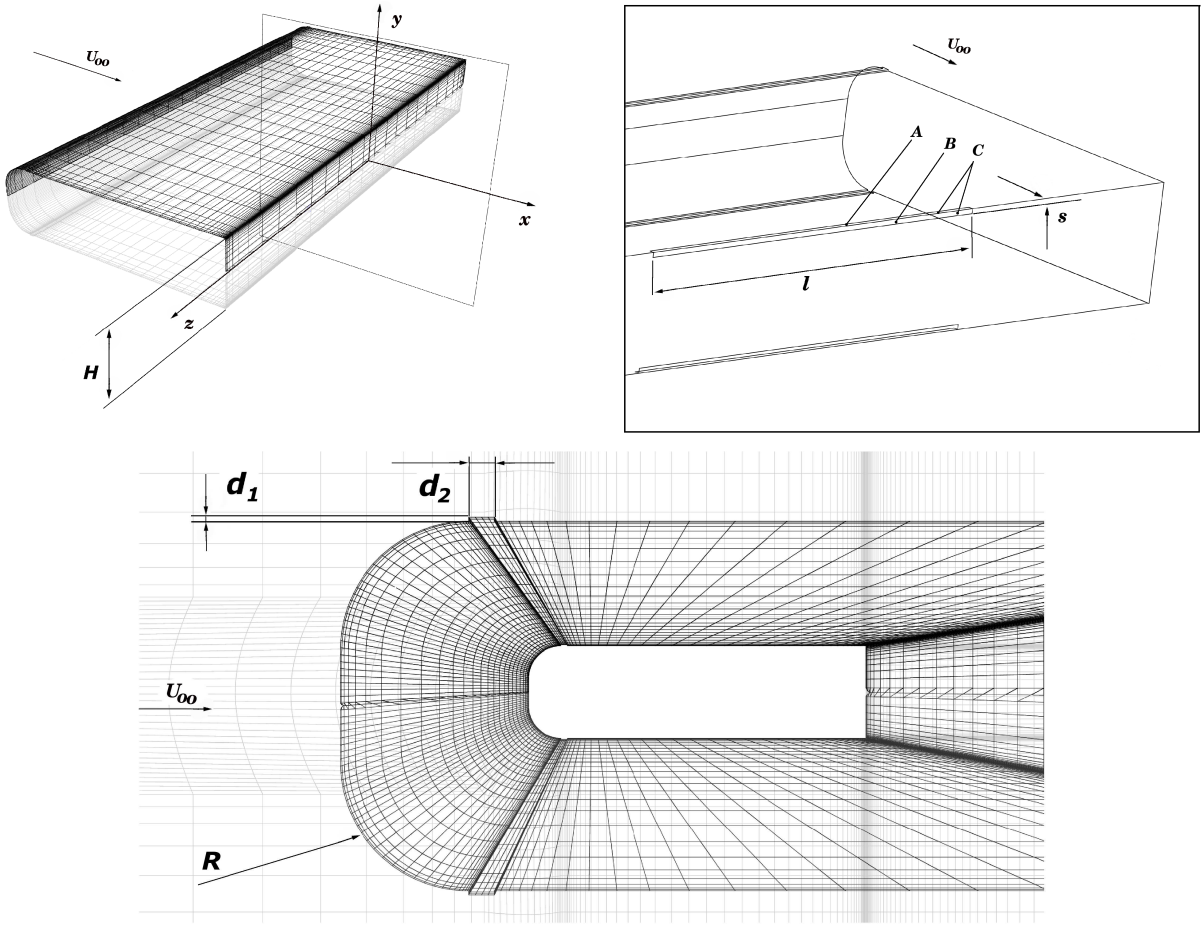

Figure 3.1: Coordinate system and reference axis; geometry of the body placed in the wind tunnel. Rear and side perspective view of the body, with the computational grid shown. Three slot configurations, A, B and C, are investigated.

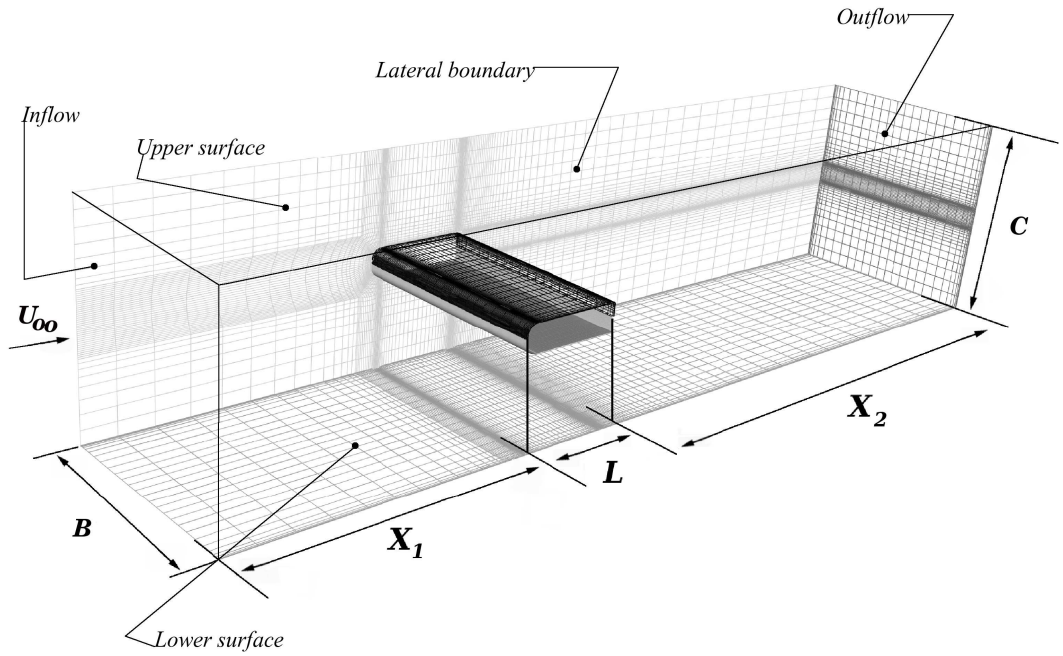

Figure 3.2: Geometry of the body placed in a wind tunnel. Front perspective view of the body, with the computational grid shown.

Actuation on the flow is made through spanwise slots with a width of $s = 0.001m$ and a spanwise length of $l = 0.250m$. [2] In the experimental model by [18],these slots are placed at the upper and lower trailing edges with an angle of 45° relatively to the streamwise direction and the outflow is normal to the slot's surface. However, since it would introduce greater complexity building a mesh for such a geometry, a decision was made to keep the geometry's section as that of an Ahmed Body with a slant angle equal to 0°. To balance this simplification, an investigation of the influence of the slot location in drag reduction is performed. A case study with a set of three different slot configurations, sketched in Fig. 3.1., is investigated:

A. The upper and lower slots are located, respectively, in trailing edge of the upper and lower surfaces of the vehicle's model.

B. The upper and lower slots are located, respectively, in the upper and lower edges of the stern's face of the model. [3]

C. The two previous configurations are blended together, that is, the slots are located both in the upper and lower faces and on the stern of the model.

[2]Please note that, for a better reader visualization, the slot width is scaled ×3 in Fig. 3.1.
[3]The stern is the rear face of the body, relatively to the flow's direction.

3.3 Boundary conditions

The inlet boundary condition is implemented using an uniform velocity profile in time. At the outlet, a Neumann boundary condition is used and the velocities are adjusted to give the required outlet flow rate to satisfy overall continuity. No-slip boundaries conditions are used on the model's surface. In the LES at $Re_h = 2 \times 10^3$, in order to decrease the cost of the computations, a slip boundary condition is chosen for both the upper and lower surfaces of the domain. However, to keep the resemblance with the experimental conditions, no-slip conditions are used at the lateral surfaces of the computational domain.

At the slots, unsteady suction and blowing is modeled using a simple analytic function as an user defined inlet boundary condition. A sinusoidal function with constant amplitude is chosen to implement oscillatory forcing with zero net flux actuation. This function is implemented with the mathematical form:

$$\vec{u}_{boundary} = Asin(\omega_A t)(cos(\phi)\hat{i} + sin(\phi)\hat{j}) \tag{3.1}$$

where $\hat{i}$, $\hat{j}$ are the unit vectors, respectively, in the x and y coordinate directions. The actuation angle, ϕ, is set to 45°. As shown in expression (3.1), no w velocity component is prescribed and, therefore, actuation is bidimensional only. The amplitude of the actuation A, that is, the actuation velocity through the slots, u_A, follows from the definition of the actuation dimensionless momentum coefficient in [18] for the *slot configurations A and B* referred in the previous section:

$$C_\mu = \frac{2s}{H}\frac{u_A^2}{U_\infty} \tag{3.2}$$

However, to keep mathematical coherence a different definition is used for the *slot configuration C*. This also allows the comparison between the slot configurations to be effective since for the same C_μ, then equal mass flow is introduced by the actuation in all cases. The momentum coefficient is defined for this slot configuration as:

$$C_\mu = \frac{4s}{H}\frac{u_A^2}{U_\infty} \tag{3.3}$$

3.4 Resolution, SGS modeling and numerical details

LES is performed on the previously described vehicle model and computational domain at $Re_h = 2 \times 10^3$. ICEM CFD was used to create a structured computational grid with a total number of nodes of $\approx 2.8 \times 10^5$. A C-type grid is built around the vehicle model and wake region, which allows an accurate control of both the boundary layer resolution in the body's wall vicinity and the shear layer downstream the body. Inside the C-type grid, special H-type grids are built around the slot's geometry that provide control of the mesh refinement in the near slot regions, without having a considerable weight on the total number of nodes of the computational mesh. H-type meshes are also used in the remaining grid topology and hyperbolic stretching is used throughout the computational mesh. Stretching ratios are retained below 1.5 in all the computational grid directions. Details of the computational grid are shown in Figure 3.3.

The number of elements in the actuation region is of remarkable importance for computing flows with implementation of active flow control. Numerical details on the computation of flows with AFC can be found mainly for airfoils [11], [12], [15]. Depending on the size and shape of the actuation slots, the number of cells per slot can vary considerably throughout the work of these authors. In the DES described in [15], the slot width contained 4 cells, while in the work by Schatz, M. et al. [13] the excitation slot is resolved using a block with 20 cells. In the LES performed by You and Moin [16], the geometry of a synthetic jet actuator was completely recreated using an unstructured mesh and the velocity boundary conditions were applied to the side wall of this modeled cavity. In the computation of the flow around a bluff body with AFC, the information concerning this detail is still rare. No detailed information is provided in [19] or [20]. As it can be observed in Figure 3.3.b., in this LES 5×9 cells were used respectively in the streamwise/transverse and spanwise directions to resolve the flow around each slot.

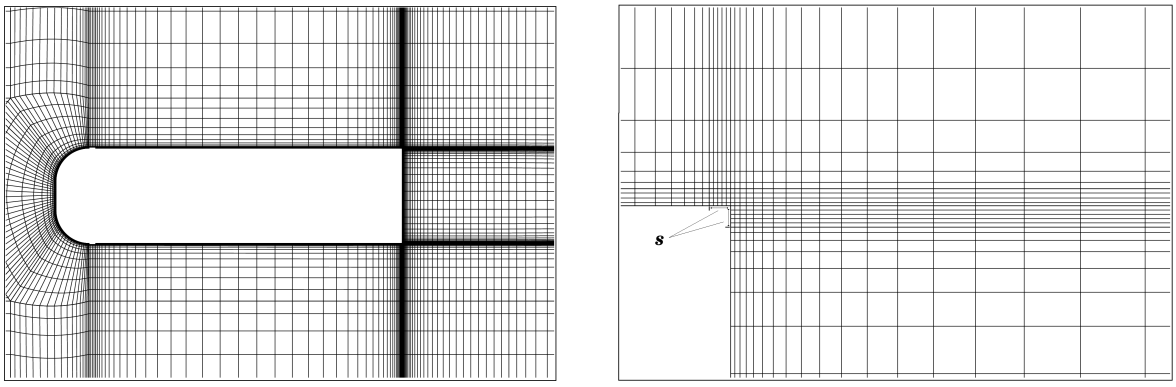

(a) **(b)**

Figure 3.3: Computational grid used to compute the flow around the vehicle model at $Re_h = 2 \times 10^3$.(a) Symmetry xy cross section showing the C-type grid used in the inner region around the body. (b) Side view detail of the H-type grids built around the slots located at the rear face's upper edge.

In all the LES performed in this work, spatial resolution is kept according to [27] to resolve the coherent structures in the near wall region. These structures can be attained using LES if $y^+ < 2$, $\Delta z^+ \approx 15 - 40$ and $\Delta x^+ \approx 50 - 150$. Associated with the LES at $Re_h = 2 \times 10^3$, the spatial resolutions of the first cell layer at the model are presented in Table 3.1, where y is the distance from the wall to the first grid node, Δz and Δx are the grid spacing, respectively, in the spanwise and streamwise directions, and u^* is the friction velocity. Since this case study was performed at a low Reynolds number, where the boundary layer thickness is small and a particularly long unsteady separation region is formed just downstream of the trip tape, special attention was given to achieve a good spatial resolution in the transverse and streamwise directions. About 4 to 5 cells are kept within the boundary layer throughout all of the model and the maximum grid spacing at the model in the streamwise direction is $\approx 0.013m$. Despite computationally expensive, the correct resolution of both the boundary layer and this long separation region is of

great importance for the accurate prediction of the body forces at this Reynolds number, where the ratio of the friction drag to the pressure drag is higher than at higher Reynolds number.

	$y^+ = yu^*/\nu$	$\Delta z^+ = \Delta z u^*/\nu$	$\Delta x^+ = \Delta x u^*/\nu$
Mean	0.27	35.0	5.6
Maximum	1.11	237.1	103.0

Table 3.1: Spatial resolution in the LES at $Re_h = 2 \times 10^3$.

STAR-CD was chosen as the solver. LES equations are discretized in space using a *Monotone advection and reconstruction scheme (MARS)*, which is a multidimensional second-order accurate differencing scheme available in STAR-CD. [4] The blending factor within MARS was set to 1, condition to use fully a central differencing (CD) scheme, and not a blend of CD with a lower order scheme, like uppwind differencing (UD). Temporal discretisation is carried out using a Three-time-level scheme, an implicit second-order accurate scheme where a quadratic variation between three time levels is used to compute the time derivative terms in the momentum equations. It requires, therefore, two old solutions for each new time step. The SIMPLE method is selected for the solution algorithm, together with a scalar algebraic multigrid (AMG) linear equation solver. Five outer iterations are allowed for each time step. The Smagorinsky model is selected as the closure model for the LES method and the Smagorinsky constant adopted is $C_S = 0.1$, following the work on external aerodynamics by [24], [25], [26], [28].

The time step was set to 0.002 seconds, i.e., $t^* = tU_\infty/H = 0.0116$. For the LES of the natural flow configuration at $Re_h = 2 \times 10^3$, the maximum Courant-Friedrichs-Levy (CFL) number is ≈ 7.3, and the mean CFL number ≈ 0.75. The same time step was kept in the LES with AFC and the maximum CFL number obtained varies from computation to computation, depending on the actuation velocity, actuation frequency and slot configuration. However, we can mention as a reference information that, for the LES that gave the maximum drag reduction at this Reynolds number, the maximum CFL number was ≈ 8.45, while the mean CFL number remained at ≈ 0.78. It was not observed that the maximum CFL number for these LES corresponds to any particular instantaneous flow condition, like the ones obtained at peak actuation suction or blowing. Since the same computational grid was used in all cases, the simulations with AFC are started from the natural flow computation after $t^* \approx 215$, a point where a fully developed turbulent flow was reached. Averaging time to obtain either the natural and the controlled time-averaged flow is $t^* \approx 232$ (20000 iterations). The computational cost of each computation using 8 Xeon 5160 CPUs was ≈ 150 hours.

[4] Discretization using pure CD in STAR-CD was attempted but abandoned, due to pressure/velocity oscillations detected in the laminar part of the flow.

3.5 Slot location

The investigation about the slot location influence on the drag force is carried out for the three different configurations described in section 3.2. All the cases are computed using the set of parameters found in [18] as the optimal set. Actuation on the flow is performed at a frequency corresponding to $St_A = 0.17$ and with an actuation velocity amplitude corresponding to the momentum coefficient $C_\mu = 0.015$. The statistics of the drag force time varying signal are summarized in Table 3.2. It can be concluded from these results that the slot configuration C is the most effective in active drag control, a configuration where the slots are placed simultaneously in the upper and lower surfaces of the body and on its stern. This can be seen through the simultaneous decrease in the mean, maximum and minimum values of C_d, when comparing them with the natural flow values. Slot configurations A and B also permit a reduction in drag but are clearly less efficient. It seems that the natural flow features are still partially dominating the wake flow and no proper control is achieved. This interference can be also concluded from the resemblance of the drag force signal corresponding to location B, presented in Fig. 3.4, with the natural flow signal, shown in Figure 3.6. It is also interesting to verify in Table 3.2 that slot location B is the one with the drag force rms value closer to the natural flow value, which seems to support the previous idea. [5] Slot location A produces the higher rms value, while location C results in an intermediate magnitude between A and B.

A detailed look is given in Fig. 3.5 to the drag force signal found from slot configuration C. Here, a harmonic function $C_d(t) = \overline{C}_d + 0.1 u_A sin(\omega_A t)$ is compared with the computed signal and two main conclusions arise. [6] First and foremost, the main frequency of the drag force signal follows the actuation frequency ω_A and this fact indicates the efficiency of the actuation in drag control. Secondly, it is observed over the signal a correlation between, on one hand, the actuation instant equivalent to peak blowing and the local drag force maximum, and on the other hand, the actuation instant corresponding to peak suction and the local drag force minimum.

	Natural Flow	Slot Config. A	Slot Config. B	Slot Config. C
$\overline{C}_d$	0.807	0.798	0.800	0.786
rms	0.0242	0.0382	0.0300	0.0341
$Maximum$	0.8738	0.9007	0.9147	0.8681
$Minimum$	0.7377	0.7158	0.7371	0.7030
$\%Reduction$	–	1.12	0.88	2.62

Table 3.2: Summary of the drag force statistics for the slot location case study, performed at $St_A = 0.17$ and $C_\mu = 0.015$.

[5] The root mean square (rms) value of the drag force signal is here computed as the square root of the signal's variance.

[6] The 0.1 scaling factor used in $C_d(t)$ is solely employed to allow a comparison of the signals features in the same scale.

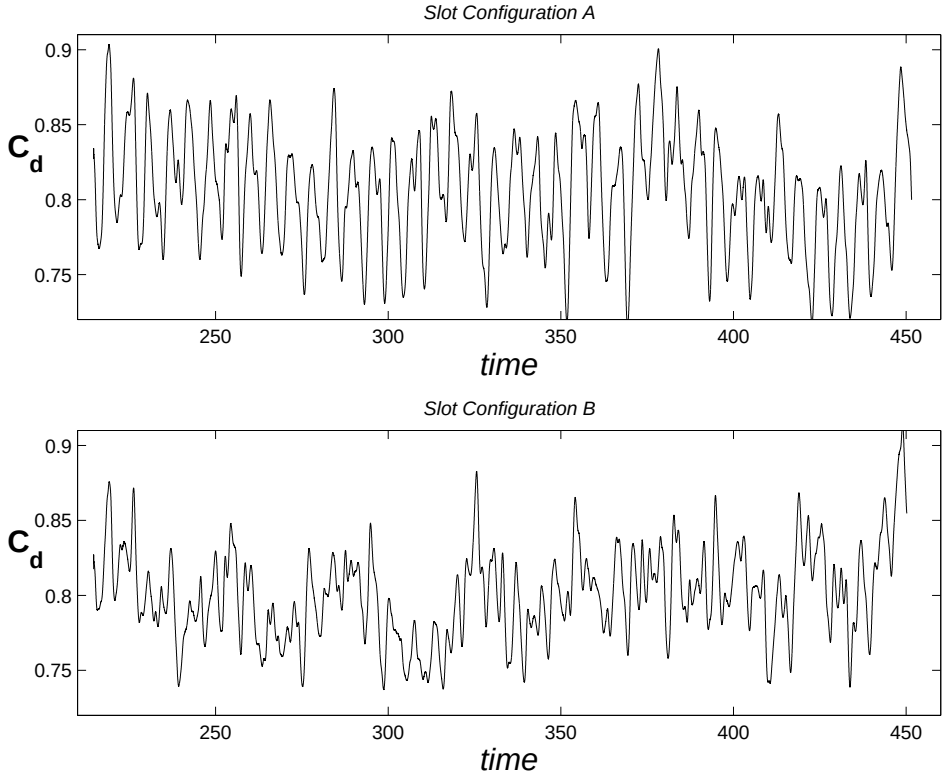

Figure 3.4: Detail of the time history C_d for the slot configurations A and B. Time is shown in dimensionless time units.

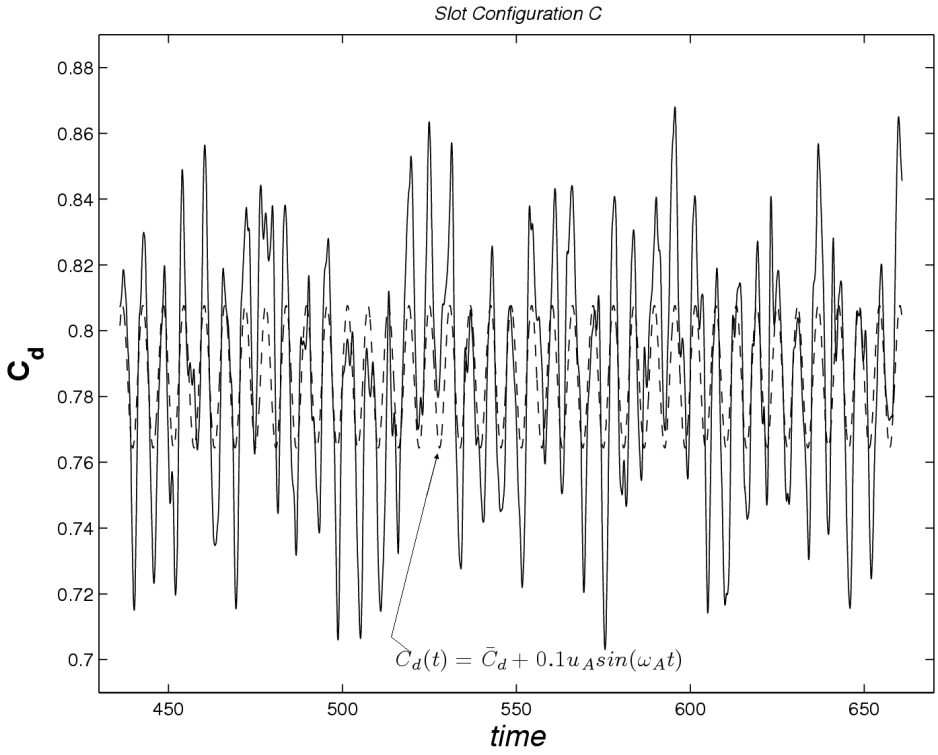

Figure 3.5: Detail of the time history C_d for the slot configuration C. Comparison with an harmonic function of frequency ω_A corresponding to $St_A = 0.17$ and mean value $\overline{C}_d$.

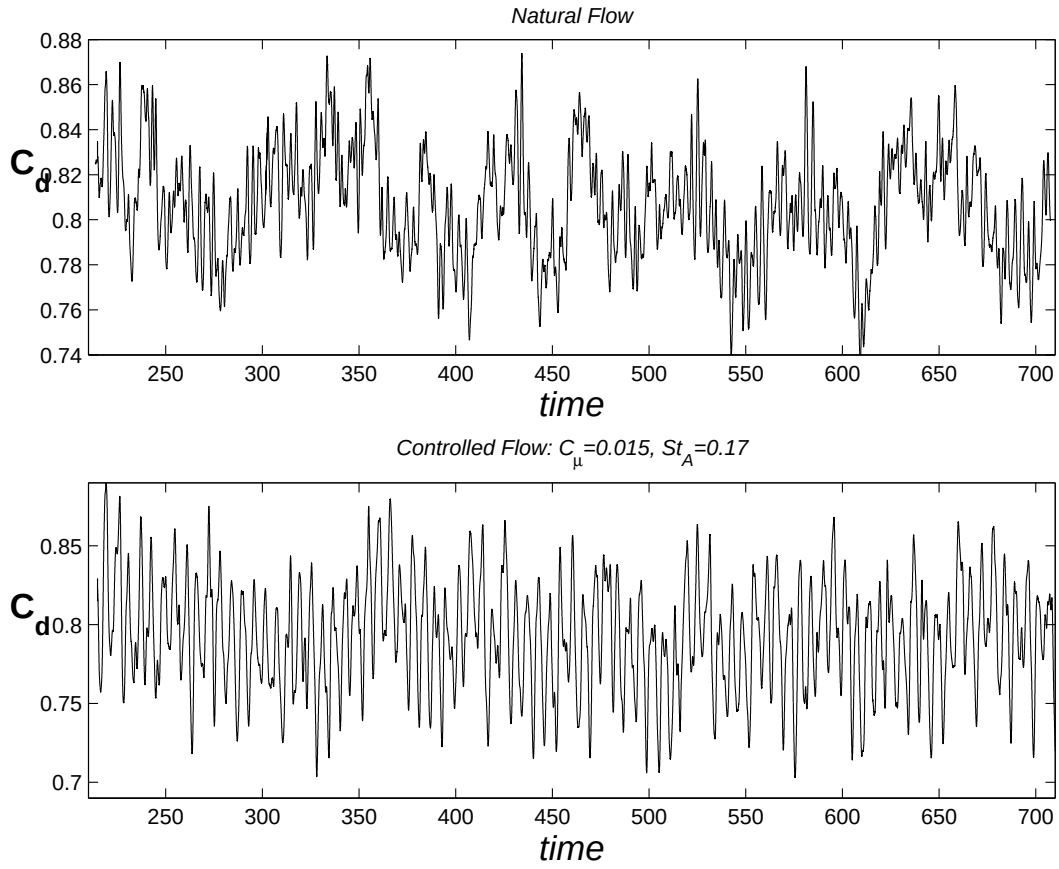

Figure 3.6: Complete time history C_d for the natural flow and the controlled flow corresponding to the slot configuration C. Time is shown in dimensionless time units.

3.6 Actuation amplitude and frequency

Due to the conclusions retrieved from the previous section, we have decided to continue with slot configuration C in continuation of the present work. The experimental work published in [18] deduced that no beneficial drag reduction is attained bellow $St_A < 0.1$ or for actuation amplitudes where $C_\mu > 0.015$. In order to comprehend the reasons for these trends, we performed a parameter sweep for several frequencies below $St_A < 0.1$ and investigated the effects of actuation velocities between $C_\mu = 0.015$ and $C_\mu = 0.12$. This section will focus in two of these investigated cases.

The drag force statistics for two cases at constant $C_\mu = 0.03$ is shown in Table 3.3, at low and high actuation frequencies, respectively, $St_A = 0.045$ and $St_A = 0.17$. The first observation retrieved from this table is that though at very different frequencies, both cases are closely related in their rms, maximum and minimum values. This indicates that the magnitude of the actuation velocity is the parameter dominating the amplitude of the drag force signal. An actuation velocity that is low will not affect much the flow and the natural flow frequencies will dominate the features of the signal, while a too high actuation velocity appears to amplify all the flow features, as it shown is in Figure 3.7 from the LES

at $C_\mu = 0.03$, $St_A = 0.17$. Both situations produce, therefore, reduced control efficiency and lower drag reduction.

	$C_\mu = 0.03$, $St_A = 0.045$	$C_\mu = 0.03$, $St_A = 0.17$
$\overline{C}_d$	0.7963	0.7949
rms	0.0478	0.0478
$Maximum$	0.8987	0.9246
$Minimum$	0.6797	0.6696
$\%Reduction$	1.39	1.57

Table 3.3: Summary of the drag force statistics for the actuation amplitude and frequency case study.

One remark should be done, however, to the previous idea. All the LES were performed with the same computational grid and solver set-up, which were previously presented. It is found that the maximum CFL number is ≈ 9.7 in the cases at $C_\mu = 0.03$, and this represents an increase in almost 15%, when compared to the maximum CFL obtained at $C_\mu = 0.015$. Even more important is the fact that, although the number of cells with higher CFL number, $CFL > 7$, constitute only $\approx 0.1\%$ of the total number of cells, all are located in the near-slot region, one or two cell layers immediately after the slot surface. This represents a problem in transient computations with AFC, since both extremely low spacial and time resolutions are needed to resolve the flow around the actuation region, without significant loss of accuracy. This lower accuracy in the near-slot region indicates that we should be careful and that further research on this topic would be required to fully confirm the previous idea. A significant decrease in the time step would be advised to be able to understand the effects of the accuracy in the near-slot region in the global solution. Of course, the cost of the computations becomes a major drawback.

The response to actuation frequencies $St_A < 0.1$ is illustrated in the top plot of Fig. 3.7. Clearly, the drag control performance is reduced and poor synchronization of the wake flow features is observed through the alternating frequencies superimposed on the dominating actuation frequency (shown by the discontinuous curve). This means that the wake instability that predominates in the natural flow around a D-shaped body is still retained in the flow at low actuation frequencies. This instability generates in the natural flow the phenomena known as vortex shedding, distinguished by an alternating sequence of vortex formation in the body's wake at characteristic frequencies. Remotion of the vortex shedding alternating frequencies is achieved by proper control at $St_A = 0.17$, as observed both in Figure 3.6 and 3.7, indicating in conclusion a synchronized vortex formation in the bluff body wake.

As a final comment, we can say that the trends observed in the experimental work [18] have been confirmed by the parameter sweep performed through our LES at this Reynolds number.

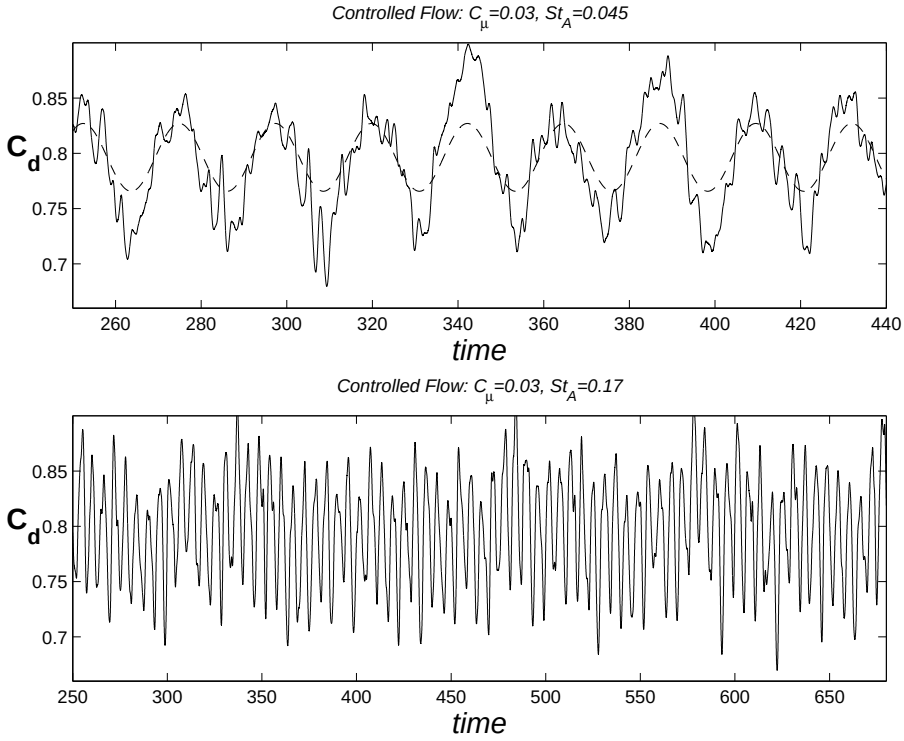

Figure 3.7: Detail of the time history C_d for the controlled flow corresponding to $C_\mu = 0.03$, $St_A = 0.045$; comparison with a harmonic function of frequency ω_A corresponding to $St_A = 0.045$ and mean value $\overline{C}_d$ (upper plot). Complete time history C_d for the controlled flow associated with $C_\mu = 0.03$, $St_A = 0.017$ (lower plot).

3.7 The instantaneous and time-averaged flows

Visualization of steady and unsteady flow patterns for both the natural and controlled flow at $Re_h = 2 \times 10^3$ is performed using critical-point concepts and methodologies, described theoretically in [29], [30].

The time-averaged natural flow at this Reynolds number is highly governed by multiple separation and reattachment regions downstream the transition tape, as indicated in Figure 3.8 through the identification of separation and attachment lines in the model's surface. Five main flow regions limited by these averaged separation and attachment lines are shown in Figure 3.10, projected into the symmetry plane $z = 0$: the flow separates immeditaly downstream of the tape forming the vortex originated in foci F_1 (counter-clockwise), reattaches through the clockwise rotating vortex F_2, separates and reattaches again forming F_3 and F_4, and finally separates forming the long counter-clockwise vortex extracted from foci F_5. The separation and attachment lengths (measured at $z = 0$) are respectively $d_1 = 0.076H$, $d_2 = 0.079H$, $d_3 = 0.161H$, $d_4 = 0.176H$ and $d_5 = 1.79H$. Due to the symmetric placement of the model in the computational domain, twin foci $F_6 - F_9$ are formed at the upper surface and are also shown in Figure 3.10. S_1 and S_2 are saddle points.

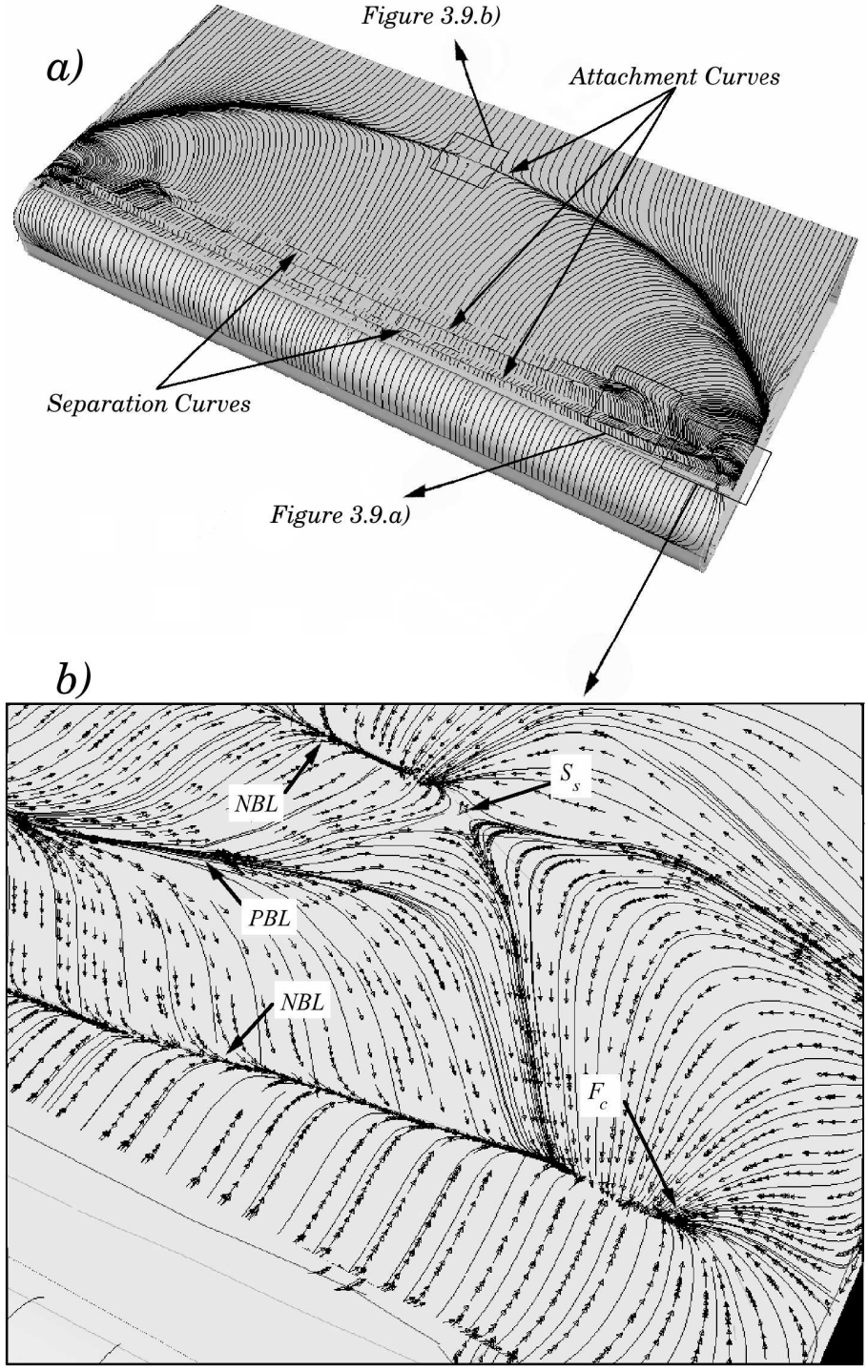

Figure 3.8: a) Time-averaged trace lines on the surface of the body, showing the separation and attachment curves. View of the front and top surfaces of the body. b) Zoom of a). The velocity vectors are plotted at a surface parallel to the body surface with an offset distance of $2.09 \times 10^{-3}H$. F_c is a stable node and S_s a saddle point. NBL and PBL are respectively separation and attachment lines.

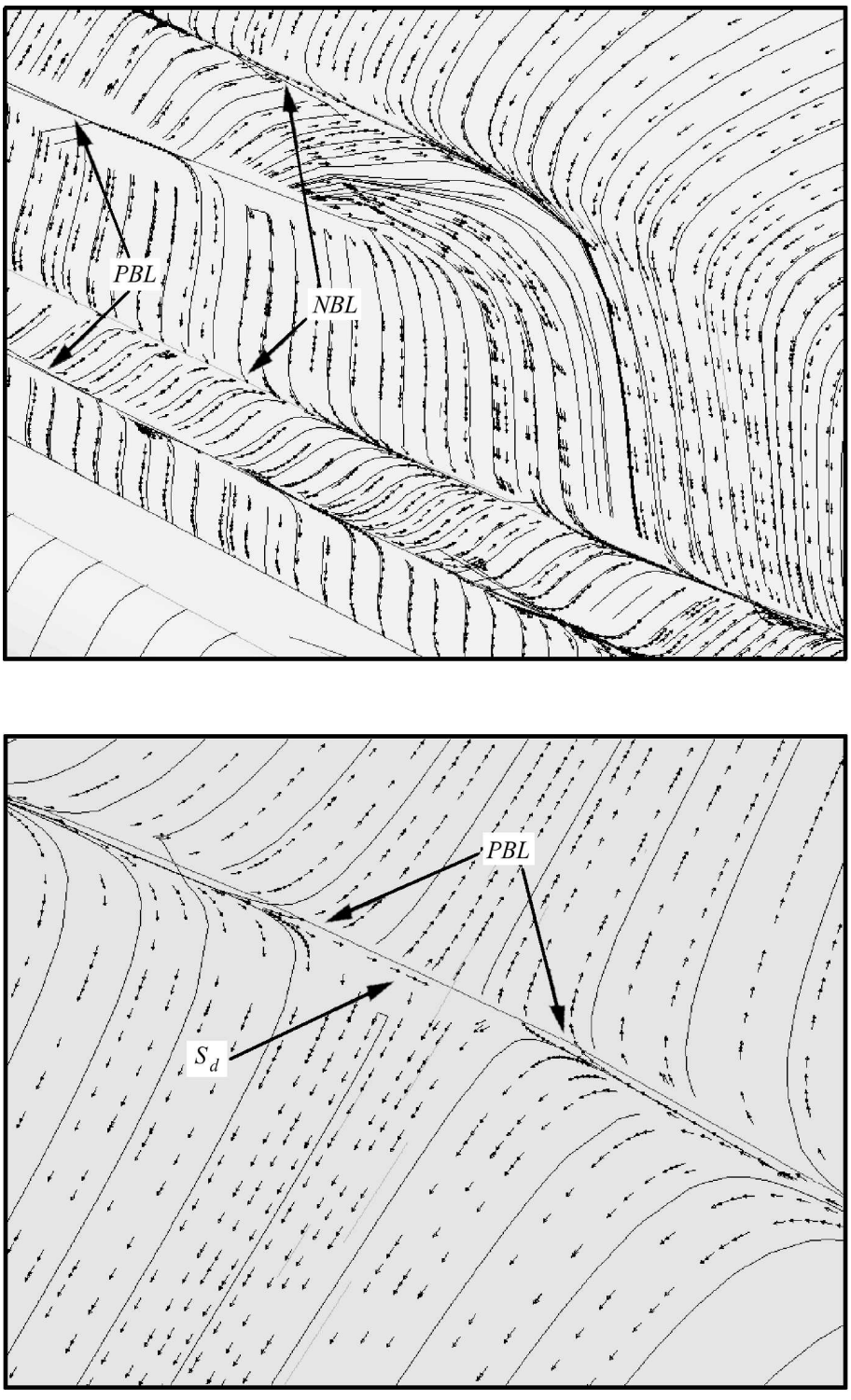

Figure 3.9: a) Zoom of Figure 3.8 a). b) Zoom of Figure 3.8 a). Time-averaged trace lines on the surface of the body. The velocity vectors are plotted at a surface parallel to the body surface with an offset distance of $2.09 \times 10^{-3} H$. S_d is a saddle point. NBL and PBL are respectively separation and attachment lines.

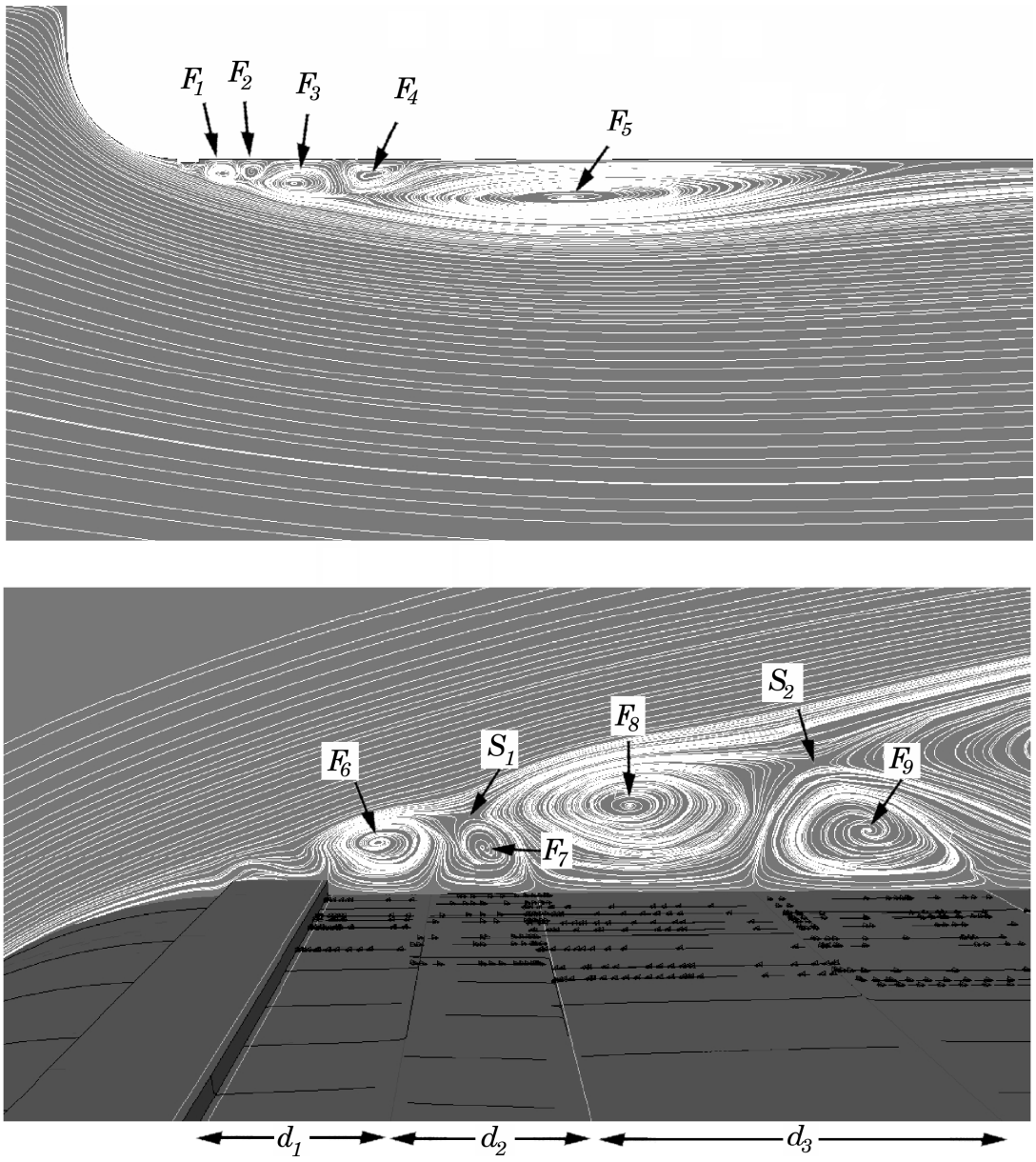

Figure 3.10: Time-averaged streamlines projected into the symmetry plane $z = 0$ of the model. $F_1 - F_9$ are foci and S_1 and S_2 are saddle points. $d_1 - d_5$ are the separation/attachment lengths measured at the symmetry plane (d_4 and d_5 are not shown here). The velocity vectors indicate the direction of rotation of the vortices associated with foci $F_6 - F_9$ and are plotted at a surface parallel to the body surface with an offset distance of $2.09 \times 10^{-3} H$.

The influence of the wind tunnel side walls is shown in the zoomed Figures 3.8 b) and 3.9. A complex flow topology is identified close to the wall in Figure 3.8 b). An independent recirculation region is formed near the saddle point S_s. A small attachment region within the first separation region downstream the tape is found upstream the stable node F_c. Figure 3.9 b) presents a zoom into the final reattachment line downstream the transition tape and the symmetry saddle point S_d.

The time-averaged large separation bubble found in the wake region of the model is presented in Figure 3.11 for the natural flow case. This region, projected into the vehicle's symmetry plane, consists of two large vortices, an upper clockwise rotating vortex and a lower counter-clockwise rotating vortex, originating respectively in the foci F_{10} and F_{11}. The free stagnation point is located at point A, with coordinates $0, -2.8 \times 10^{-3}, 0$, indicating perfect symmetry at this plane. The same symmetry is found in the location of the saddle point D. Differences between the locations of foci F_{10} and F_{11} are found to be $\approx 2.9\%$ and $\approx 1.6\%$, respectively in the x and y coordinates at this plane. Two half-saddle S_4 and S_5 are located at the upper and lower vertices of the model's rear face. The total mean separation bubble length is $X_n \approx 1.33H$.

Bearing in mind these main time-averaged flow features of the natural flow around the vehicle model, investigation of the instantaneous flow provides the mean to understand how drag force reduction is achieved through the harmonic actuation introduced in the present work. The natural flow is governed by an alternating sequence of strong vortex formation, originated from the upper and lower trailing edges at characteristic frequencies. The phenomena is shown in Figure 3.12 a) and 3.13 a), where foci N_1 and N_4 are the origin of high amplitude vortices at two independent flow instants. Also observed in these figures, as a result of producing strong alternating instabilities in the near-wake region, the vortices roll-up produces a highly bent shear layer and a momentum interaction between the upper and lower shear layers. The shear layer interference occurs one to two body heights downstream of the coordinate system origin and produces the wake instability known as Von Kármán vortex street or vortex shedding, visualized both by the roll-up of a third swirling vortex (foci N_3 in Figure 3.12 and N_6 in Figure 3.13) and by the characteristic pattern of the streamlines. This wake phenomena achieves the maximum amplitude at dominant Strouhal numbers, usually within the range of $0.2-0.26$ for Ahmed type bluff bodies, [18]. The corresponding instantaneous pressure coefficient plotted in the symmetry plane $z = 0$ along the body's height and at several streamwise planes is shown in Figure 3.12 b) and Figure 3.13 b). Even very close to model's rear surface, at $x/H = 0.014$, the attained pressure distribution is greatly asymmetric, with a pressure coefficient minimum at $C_p \approx -0.7$, associated with the large vortex location. The asymmetry as well as the magnitude of the pressure minimum grow as we move further from the wall.

As it was demonstrated in section 3.5, harmonic actuation in the flow's wake region at $St_A = 0.17$ and $C_\mu = 0.015$ successfully synchronizes the drag force response with the actuation frequency and local maximum and minimum drag force values were found to be connected respectively with peak blowing and peak suction. This has led to a drag force reduction. Figures 3.14 and 3.15 unveil why. The alternating sequence of vortex formation, characteristic of the natural flow, is suppressed in the controlled flow and this is the main mechanism responsible for drag reduction. This conclusion arises from the

observation of the typical flow features at both peak suction and peak blowing actuation instants, presented respectively in Figure 3.14 a) and Figure 3.15 a). Two synchronized vortices with similar amplitude (at foci C_1/C_2 and foci C_4/C_5) are formed at both instants and the momentum interaction between the upper and lower shear layers is reduced. It is observed that vortex shedding is delayed further downstream and its amplitude is reduced and, consequently, it is concluded that the wake instability is reduced through harmonic actuation. This idea is confirmed by the corresponding instantaneous pressure coefficient, shown in Figure 3.14 b) and Figure 3.15 b), where it can be observed the existence of a considerably more uniform pressure distribution throughout the near-wall wake region. The two synchronized vortices present in the controlled flow are particularly weak when peak suction is attained. This is responsible by the uniform pressure distribution at $t^* = 710.47$, where the average pressure coefficient along the model's height is close to $\overline{C}_p \approx -0.53$ at the symmetry plane and at $x/H = 0.014$. The higher pressure recovery attained leads to the lower drag force coefficient observed at peak suction, as illustrated by the value of $C_d = 0.72$ at $t^* = 710.47$. These conclusions have been supported in the observation of similar results at equivalent flow instants. At peak blowing instants, it is the amplitude of the two wake vortices that drives the pressure on the model's rear surface to lower values, thus producing higher drag forces as exemplified at $t^* = 689.0$ by drag force value of $C_d = 0.82$. But, the net effect of the control strategy is proven to be beneficial to drag reduction due, therefore, to the synchronized vortex formation in the wake region.

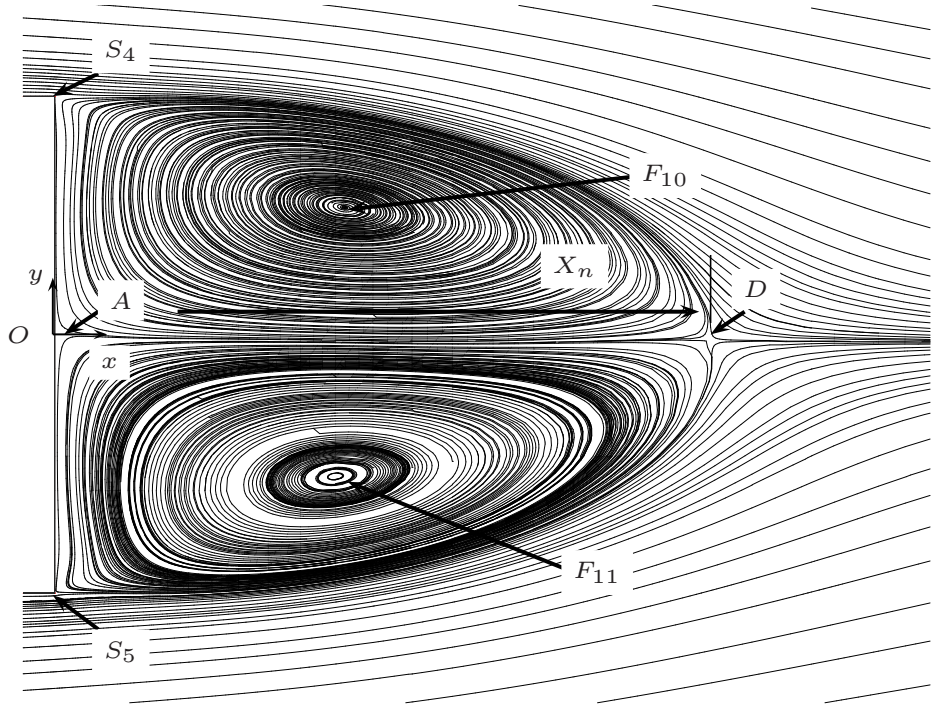

Figure 3.11: Time-averaged streamlines projected into the symmetry plane $z = 0$ of the vehicle for the LES of the natural flow at $Re_h = 2 \times 10^3$. View of the wake region. A is the stagnation point in the rear face of the model. F_{10} and F_{11} are foci corresponding respectively to the upper and lower vortices and D is the saddle point. S_4 and S_5 are half-saddles. The separation bubble length in the rear of the model is indicated as X_n.

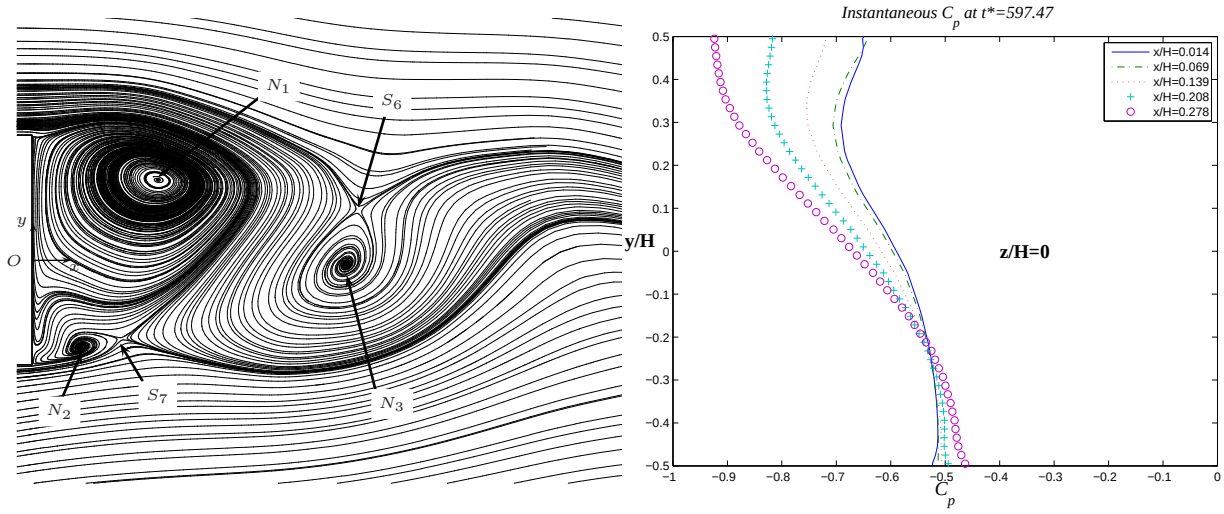

a) *b)*

Figure 3.12: a) Instantaneous streamlines projected into the symmetry plane of the natural flow at time $t^* = 597.47$. View of the wake region. N_1 and N_2 are foci associated respectively with the large upper edge clockwise vortex and the small lower edge counter-clockwise vortex. S_6 and N_7 are saddles. Downstream of the separation bubble, foci N_3 arises from the Vortex Shedding formation. b) Pressure coefficient along the model's height, at five x/H locations and at $t^* = 597.47$.

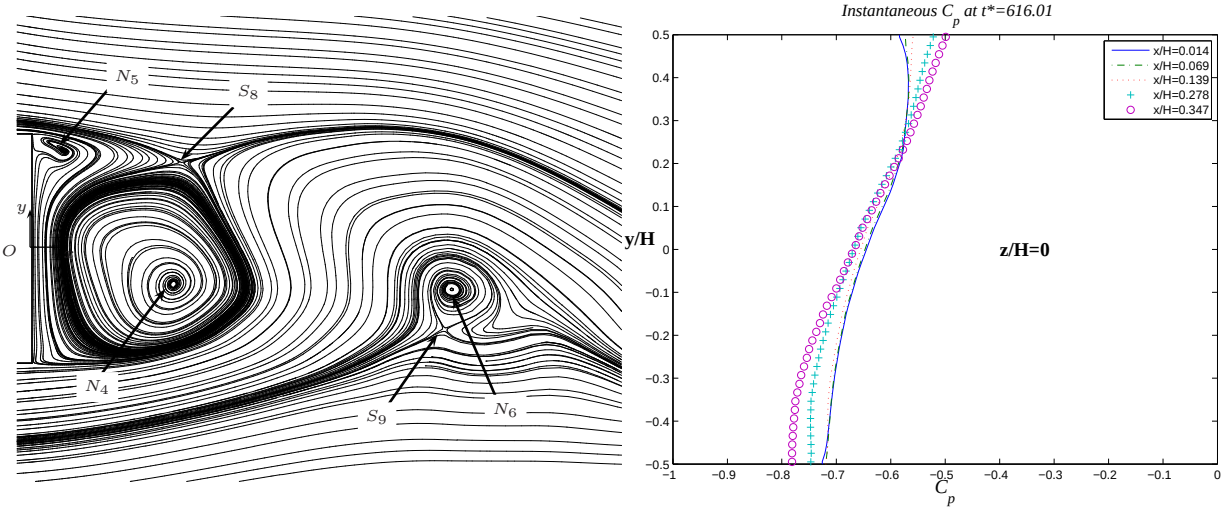

a) *b)*

Figure 3.13: a) Instantaneous streamlines projected into the symmetry plane of the natural flow at time $t^* = 616.01$. View of the wake region. N_4 and N_5 are foci associated respectively with the large lower edge counter-clockwise vortex and the small upper edge clockwise vortex. S_8 and N_9 are saddles. Foci N_6 arises from the Von Kármán vortex street formation. b) Pressure coefficient along the model's height, at five x/H locations and at $t^* = 616.01$.

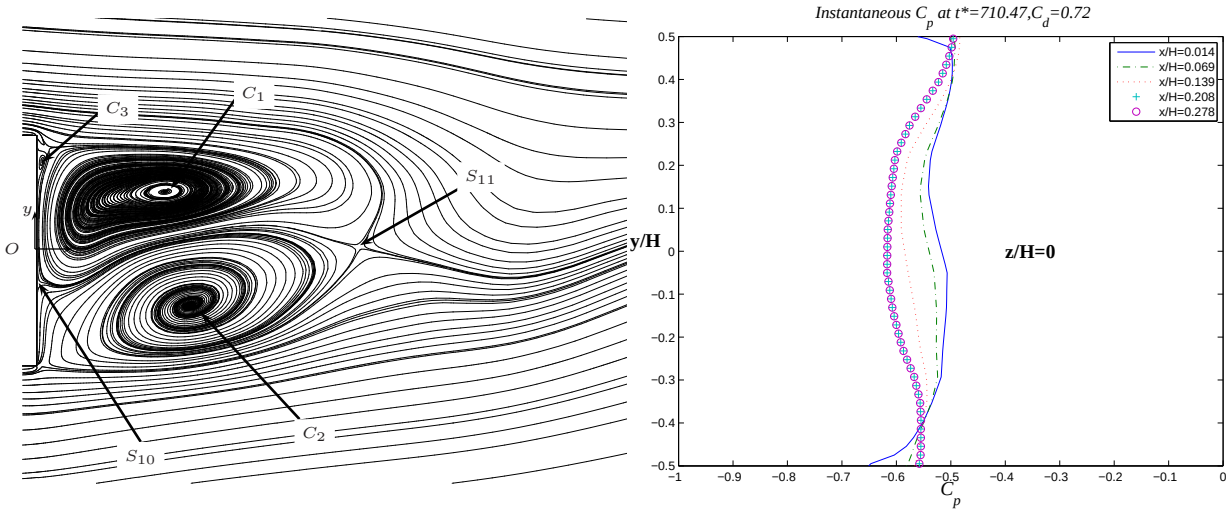

a) *b)*

Figure 3.14: a) Instantaneous streamlines projected into the symmetry plane of the controlled flow at time $t^* = 710.47$, corresponding to a peak suction instant. View of the wake region. C_1 and C_2 are foci, linked respectively to a clockwise and counter-clockwise vortex. A thin counter clockwise rotating vortex is observed at foci C_3. S_{10} is a stagnation point and S_{11} is a saddle. b) Pressure coefficient along the model's height, at five x/H locations and at $t* = 710.47$.

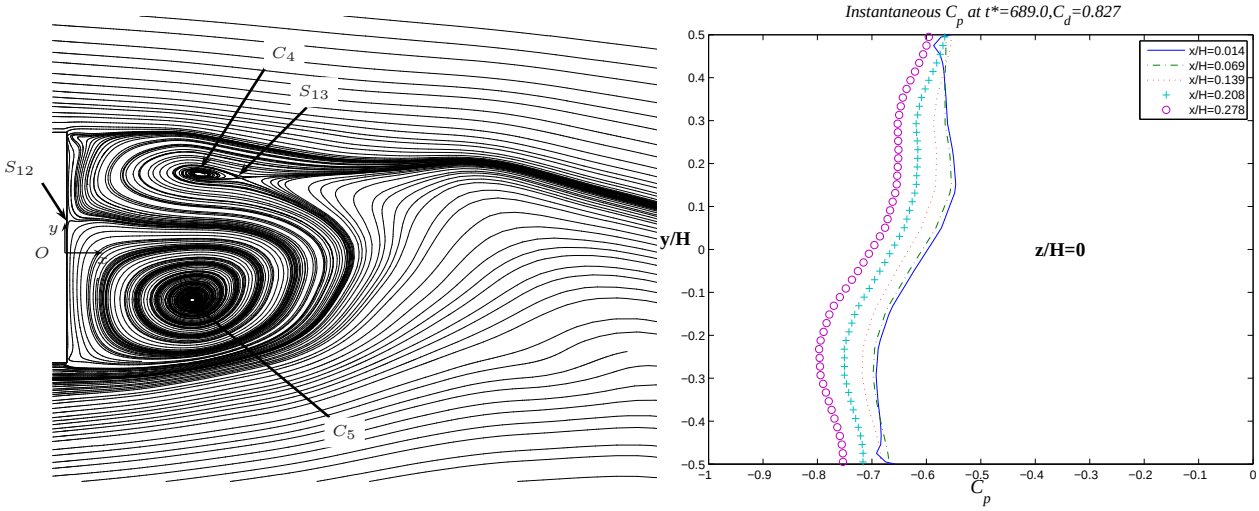

a) *b)*

Figure 3.15: a) Instantaneous streamlines projected into the symmetry plane of the controlled flow at time $t^* = 689.0$, corresponding to a peak blowing instant. View of the wake region. C_3 and C_4 are foci. The upper vortex is clockwise and lower is counter-clockwise. S_{12} a stagnation point and S_{13} is a saddle. b) Pressure coefficient along the model's height, at five x/H locations and at $t* = 710.47$.

A detailed look is finally given to the time-averaged controlled flow obtained with the actuation parameters $St_A = 0.17$ and $C_\mu = 0.015$. Figure 3.16 illustrates that the mean flow topology is similar to that of associated with the mean natural flow in Figure 3.11, with two symmetric vortices originated at foci G_1 and G_2, a symmetrically positioned saddle point E and stagnation point B and two half-saddles at the upper and lower edges of the model's rear face. The main difference is actually in the streamwise location of these critical points. We found that the separation bubble length is $X_c = 1.31H$ and this corresponds to a reduction of 1.5% in the bubble size. Along the spanwise direction, the separation bubble size varies considerably due to the existence of a recirculation region with $X_r = 1.1H$, where a counter-clockwise rotating vortex is originated at foci G_3. Figure 3.17 illustrates these features and the time-averaged streamlines projected on the rear face of the model indicate the three-dimensionality of the separation bubble in the spanwise direction. An unstable node is found at Z. The wind tunnel side walls thus promote a three-dimensional time-averaged wake. The three-dimensional effects are better visualized in Figure 3.18, where it is shown how the spanwise vortex near the side walls *pulls* the location of the foci G_4 and G_5 further downstream. In fact, the separation length bubble at $z/H = -2.5$ is $X_d = 1.52H$ and this represents an increase of $\approx 16\%$ relatively to the bubble size at the symmetry plane.

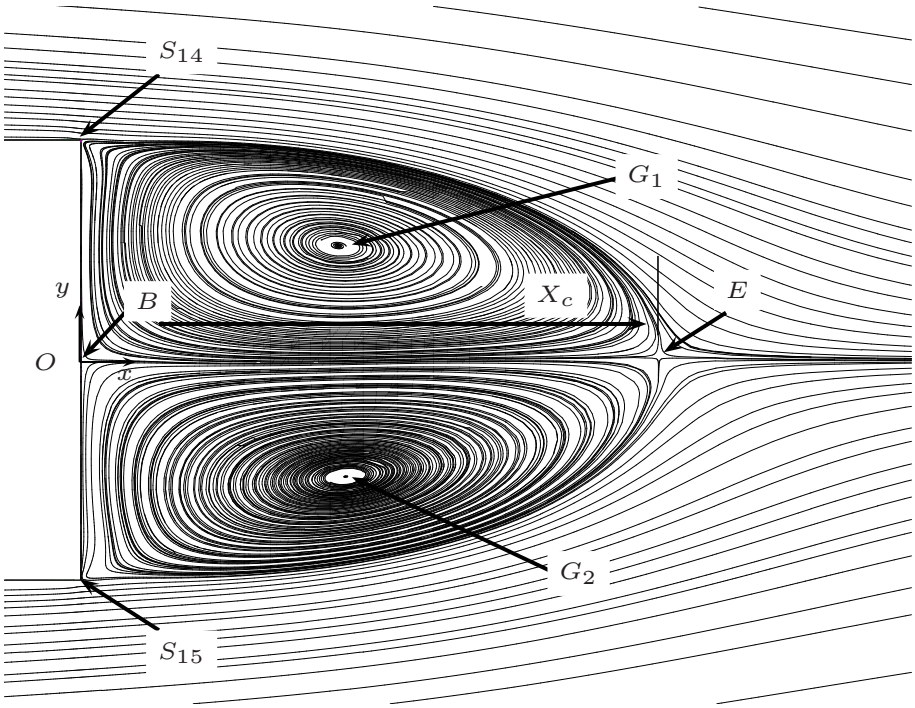

Figure 3.16: Time-averaged streamlines projected into the symmetry plane $z = 0$ of the vehicle for the LES of the controlled flow at $Re_h = 2 \times 10^3$. View of the wake region. G_1 and G_2 are foci corresponding respectively to the upper (clockwise) and lower (counter-clockwise) vortices and E is the saddle point. S_{14} and S_{15} are half-saddles. B is the stagnation point in the rear face of the model. The separation bubble length in the rear of the model is indicated as X_c.

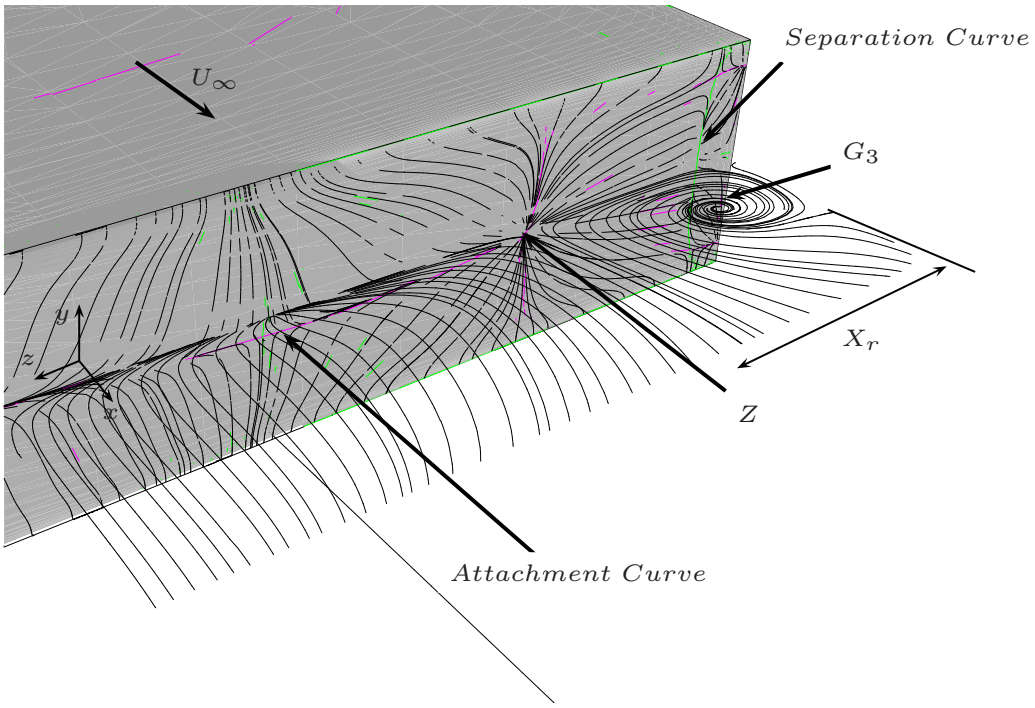

Figure 3.17: Controlled flow time-averaged streamlines projected into the rear face of the body and into plane $y = 0$. Perspective view of the model's stern and wake region. Attachment and separation lines are indicated. A counter-clockwise vortex near the side-wall of the wind tunnel is originated at foci G_3. Z is an unstable node.

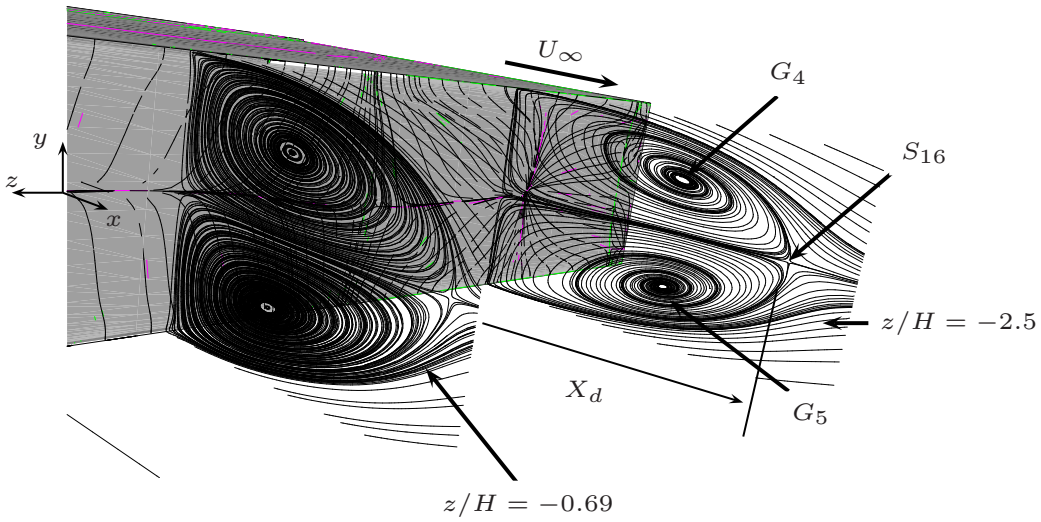

Figure 3.18: Controlled flow time-averaged streamlines projected into the rear face of the body and into planes $z/H = -0.69$ and $z/H = -2.5$. Perspective view of the model's stern and wake region. G_4 and G_5 are foci and S_{16} is a saddle, at plane $z/H = -2.5$. X_d is the separation bubble length at $z/H = -2.5$.

The curvature in the attachment curve that is visible in Figure 3.17 compels us to conclude that the averaging time was not long enough to obtain a statically perfect time-averaged flow. Further averaging would be required therefore to attain this purpose. The asymmetric time-averaged pressure coefficient profile observed for the natural flow case in Figure 3.19 also supports this conclusion. A quite long required averaging time is a consequence of the complex three-dimensional and highly separated flow topology found at this Reynolds number. However, the investigation at $Re_h = 2 \times 10^3$ has clearly demonstrated the mechanisms supporting drag force reduction and the main flow features have been captured both for the natural and the controlled flow. The parameter sweep that we performed would also have been impossible at higher Reynolds number and this study has allowed us to gain considerable understanding about the computational implementation of active flow control. The success of drag control is also demonstrated in the time-averaged pressure recovery along the spanwise direction of the model's stern that is visible throughout Figure 3.19.

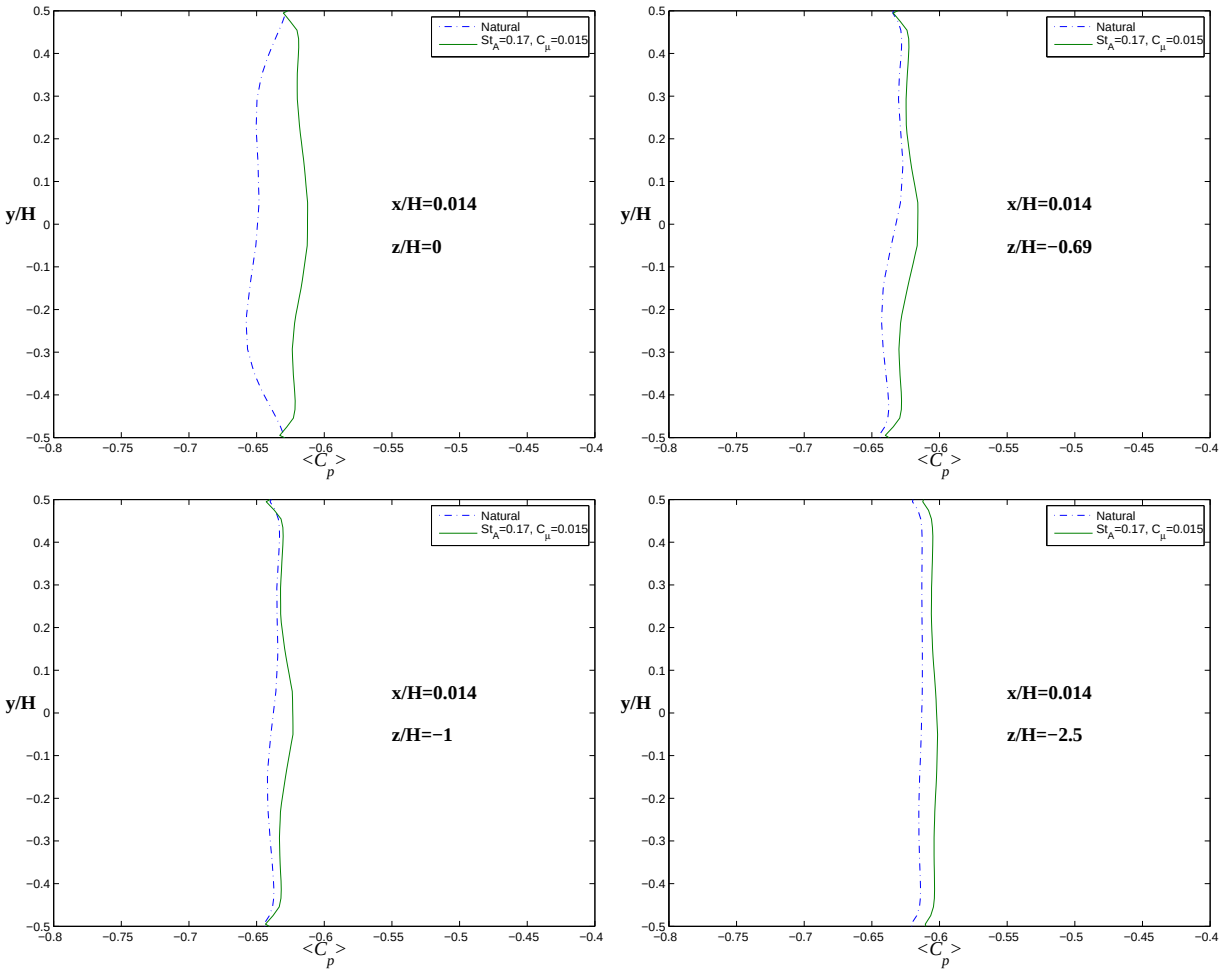

Figure 3.19: Comparison between the natural and the controlled flow time-averaged pressure coefficient. $\overline{C}_p$ is plotted along the model's height at $x/H = 0.014$ and at four spanwise locations $z/H = 0$, $z/H = -0.69$, $z/H = -1$ and $z/H = -2.5$.

Chapter 4

Making LES of the flow around a simplified vehicle with active control

This chapter presents the efforts to make the LES of the flow around a simplified vehicle with active flow control at a considerably more interesting Reynolds number, from the engineering point of view. The effectiveness of the control strategy is discussed from the comparison of the drag force results between the natural and the controlled flow. The ability of LES to describe in detail the transient nature of the physics of these flows is finally exploited to understand the mechanisms underlying active drag control.

4.1 Geometry, boundary conditions and resolution

LES of the flow around a simplified vehicle mounted in a wind tunnel is performed at $Re_h = 2 \times 10^4$. The circular rods used to mount the model in the wind tunnel's test section from [18] are included into the geometry of the body, already introduced in *section* 3.2. The revolution axis of the two rods, collinear with the y axis, are located at $x = -1.79H$ and $z = \pm 2.389H$. The rods are extended from the lower surface of the body to the lower surface of the computational domain. The diameter is $D = 0.01m$ [31]. Figure 4.1. depicts the new geometry and the computational domain dimensions.

An uniform velocity profile constant in time is used as the inlet boundary condition. At the domain's exit, a Neumann boundary condition is implemented. The velocities at the outlet are adjusted so that overall continuity is verified. In order to fully reproduce the experimental conditions, the top and bottom surfaces and the lateral surfaces of the computational domain are treated as no-slip boundary conditions. No-slip is also prescribed to the vehicle's surface. Grid resolution is, therefore, constructed to adequately resolve the boundary layers on all of these walls. Actuation through the slots occurs with $C_\mu = 0.015$ and with the actuation frequency corresponding to $St_A = 0.17$. Here, the momentum coefficient follows the definition:

$$C_\mu = \frac{4s}{H} \frac{u_A^2}{U_\infty} \tag{4.1}$$

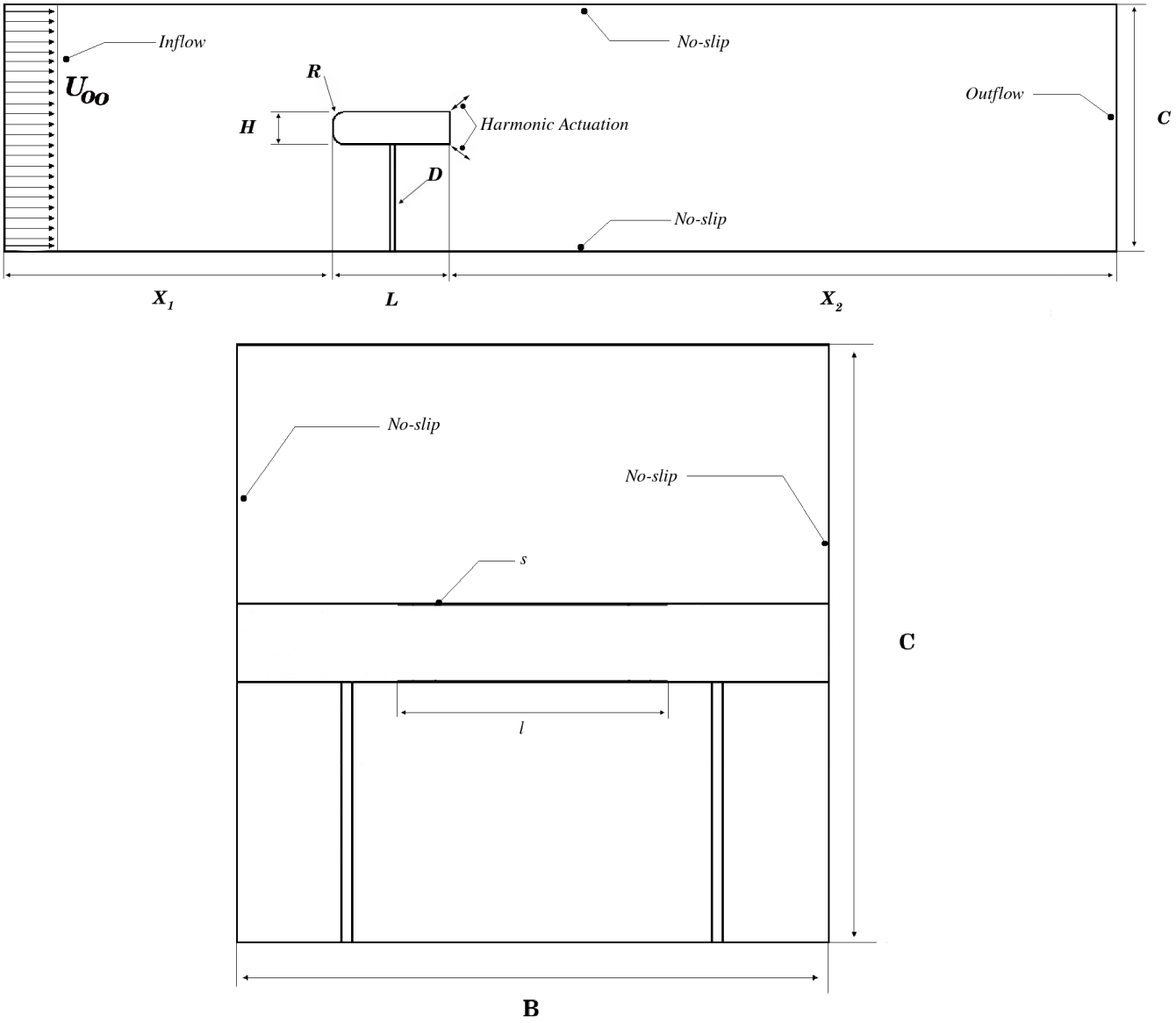

Figure 4.1: Geometry of the body placed in the wind tunnel, for the flow computation at $Re_h = 2 \times 10^4$. Side and rear view. Body and computational domain shown.

Oscillatory forcing in time at 45° with the streamwise direction is, thus, implemented as an inlet boundary condition using:

$$\vec{u}_{slot} = u_A sin(\omega_A t)(cos(\phi)\hat{i} + sin(\phi)\hat{j}) \tag{4.2}$$

To accommodate all the described changes, a new computational grid for this geometry and Reynolds number is created. An O-grid is built around each rod, while the remaining grid topology is conserved, i.e, the C-grid around the vehicle model and wake and the H-type grids around the actuation slots. Figure 3.2. illustrates some new details of the computational grid. As it is pointed out in chapter 3, drag force control is only achieved from *slot configuration C*. This configuration is therefore adopted and 5×54 cells are placed on each slot's surface to resolve the flow around it. Near-wall spatial resolution

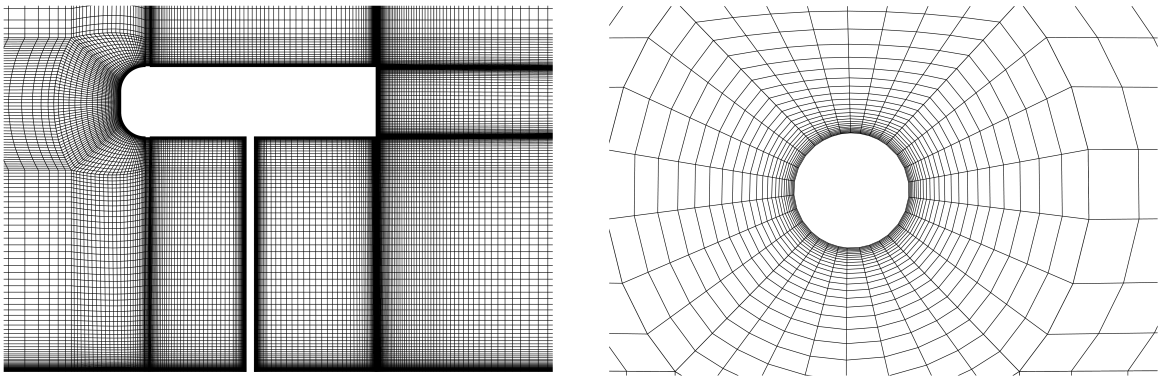

a) *b)*

Figure 4.2: Computational grid used to compute the flow around a simplified vehicle at $Re_h = 2 \times 10^4$. a) xy cross section at $z = 2.389H$ showing the C-type grid created around the body and the O-type grid built around the rods. b) Top detail view of the O-grid, at $y = -3.854H$.

is also sustained from [27] to resolve the coherent structures generated in that region. Approximately 8 to 9 grid nodes are preserved within the boundary layer thickness. The spatial resolutions of the first cell layer attached to the model's surface are given in Table 4.1. The total number of nodes is $\approx 5.5 \times 10^6$ for the computational grid conceived to resolve the flow. Relatively to the solver, discretization schemes and to SGS modeling, identical set-up to the one described in *section* 3.4 was employed. The physical time step is 1×10^{-4}, corresponding to $t^* = tU_\infty/H = 0.0058$. The maximum CFL number is ≈ 8.5, while its mean value is ≈ 0.28, for the natural flow computation at $Re_h = 2 \times 10^4$. The CFL number is smaller than one in approximately 96.5% of the cells. The same computational grid is used both for the natural flow and the controlled flow LES, and both simulations are performed from scratch. Averaging time to obtain the natural time-averaged flow is $t^* \approx 106.4$ (≈ 18300 iterations). The controlled time-averaged flow is obtained after approximately $t^{\approx} = 93.4$ (≈ 16100 iterations). The computational cost of each LES using 20 Xeon 5160 CPUs was ≈ 600 hours.

	$y^+ = yu^*/\nu$	$\Delta z^+ = \Delta z u^*/\nu$	$\Delta x^+ = \Delta x u^*/\nu$
Mean	1.06	30.02	13.78
Maximum	4.78	146.63	146.32

Table 4.1: Spatial resolution in the LES at $Re_h = 2 \times 10^4$.

4.2 Drag control results

Two main goals are achieved through the computation of the natural and the controlled flow at $Re_h = 2\times10^4$: firstly, a comparison between the LES and the available experimental results; secondly, the corroboration of the efficiency of the actuation strategy for drag force control and reduction. The drag force statistics presented in Table 4.2 indicate a 10.5% drag reduction and this represents an increased control efficiency at this Reynolds number, when compared with the drag force results obtained for the case-study described in *chapter 3*. The complete drag force history shown in Fig. 4.3 illustrates the effects of harmonic actuation in the drag signal. The *controlled* variable, the drag force, follows the frequency imposed by the *controller*, the harmonic actuation in the wake. This linear relationship is typical of 1^{st} Order control systems. Comparison between the time-averaged pressure distributions very close to the model's rear face, at $x/H = 0.014$, is shown in Fig. 4.4 for different spanwise locations $z/H = 0$, $z/H = 0.35$, $z/H = 1.0$ and $z/H = 2.5$. The controlled flow time-averaged pressure coefficient profile is observed to remain considerably uniform and constant, close to $\overline{C}_p = -0.7$, along the spanwise direction of the model. Thus, it can be depicted from the previous fact the two-dimensional nature of the main wake flow features at this Reynolds number. Summarizing, the drag force signal control and the existing pressure recovery in the near-wake region of the actuated flow, observed in Fig. 4.4, support the evidence of an efficient active drag control.

LES validation is performed using the present investigation's reference experimental results [32], [33]. Available experimental drag force results from [32] are reproduced in Table 4.2. Though the experimental data is only available for $Re_h = 2.3\times10^4$, $\approx 4\%$ difference is obtained between the computed and the experimental natural flow drag coefficient. Particle Image Velocimetry (PIV) data obtained at $Re_h = 2 \times 10^4$ and received from [33] has also been used for results validation. Two thousand instantaneous uncorrelated PIV time samples have been used to obtain the experimental time-averaged base flow; and one thousand six hundred uncorrelated measurements for the controlled flow case. The PIV data received is unpublished and, therefore, no detailed information is available about the data validation algorithms used in the measurements. Regular statistical averaging was thus performed, i.e., no spurious vectors replacement or interpolation algorithms were used in the present work. These algorithms are often used in PIV data post-processing.

	LES at $Re_h = 2 \times 10^4$		Exp. at $Re_h = 2.3 \times 10^4$	
	Natural	Controlled	Natural	Controlled
$\overline{C}_d$	1.02	0.91	0.98	0.83
rms	0.029	0.054	–	–
$Maximum$	1.102	1.035	–	–
$Minimum$	0.958	0.784	–	–
$\%Reduction$	–	10.5	–	15.0

Table 4.2: Summary of the drag force statistics for the LES performed at $Re_h = 2 \times 10^4$. Comparison with the experimental data available at $Re_h = 2.3 \times 10^4$

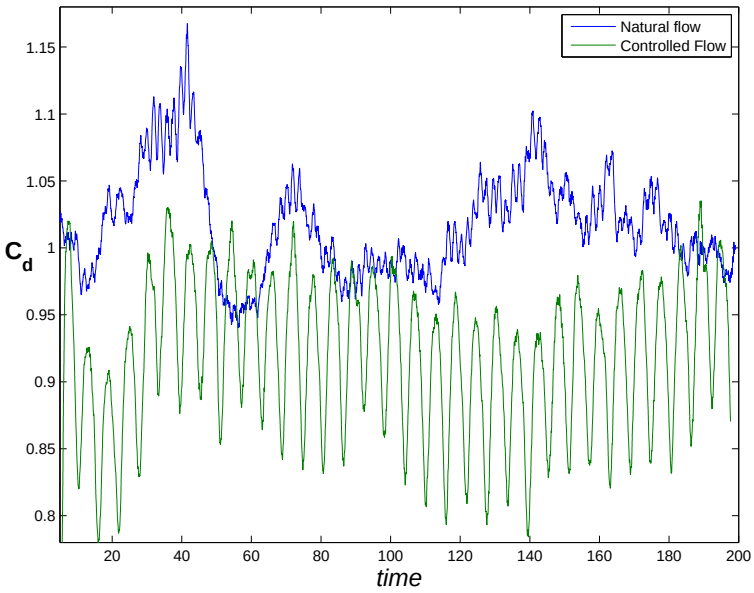

Figure 4.3: Time history C_d for the natural and controlled flow at $Re_h = 2 \times 10^4$. Time is shown in dimensionless time units.

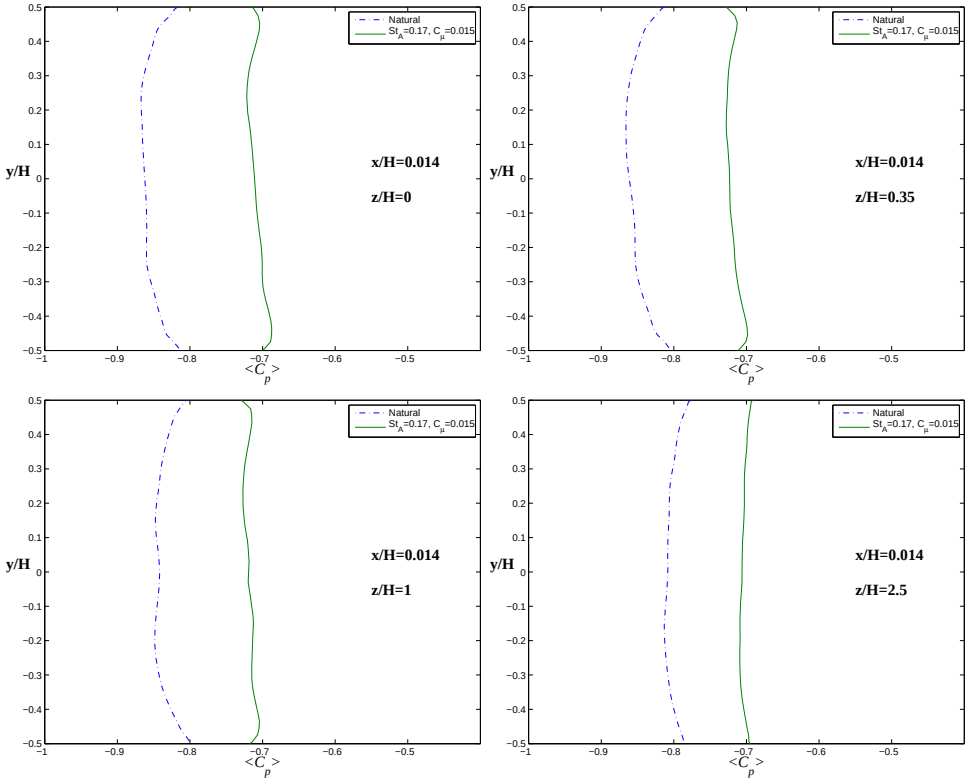

Figure 4.4: Comparison between the natural and controlled flow time-averaged pressure coefficient. $\overline{C}_p$ is plotted along the model's height at $x/H = 0.014$ and at four spanwise locations $z/H = 0$, $z/H = 0.35$, $z/H = 1$ and $z/H = 2.5$.

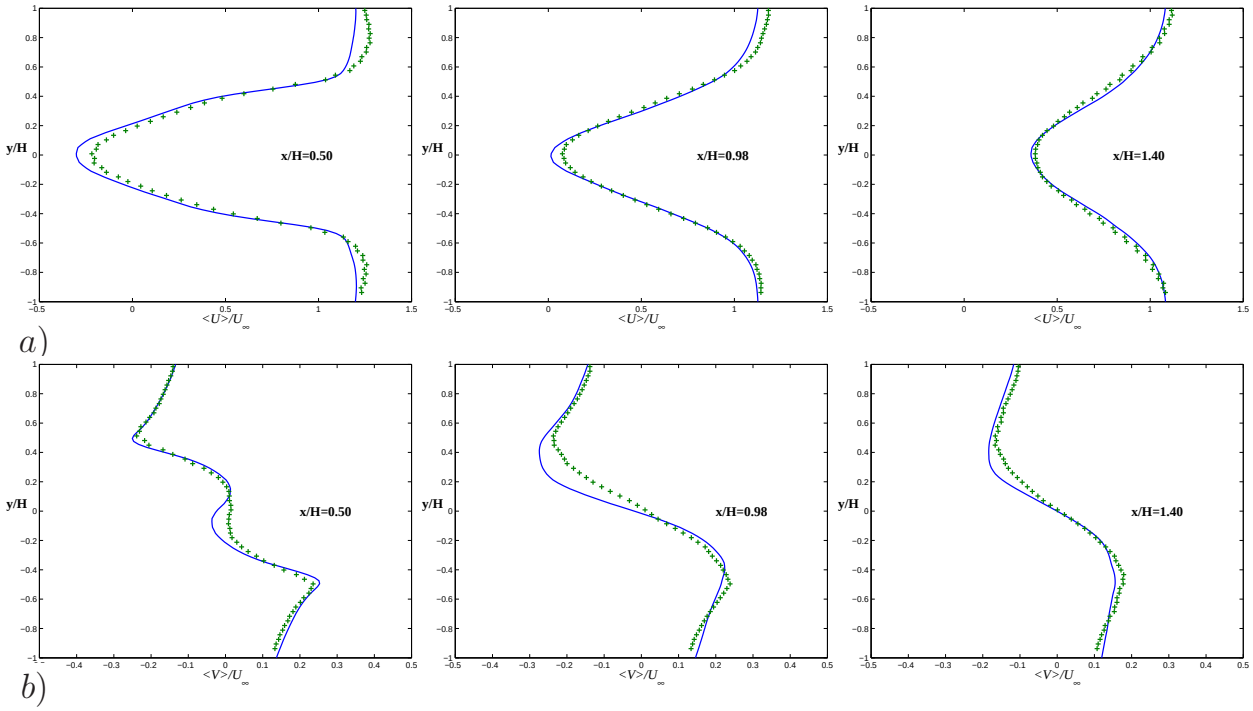

Figure 4.5: Natural flow time-averaged velocity profiles at three downstream locations at $z = 0$. LES data (solid line); PIV data (symbols).

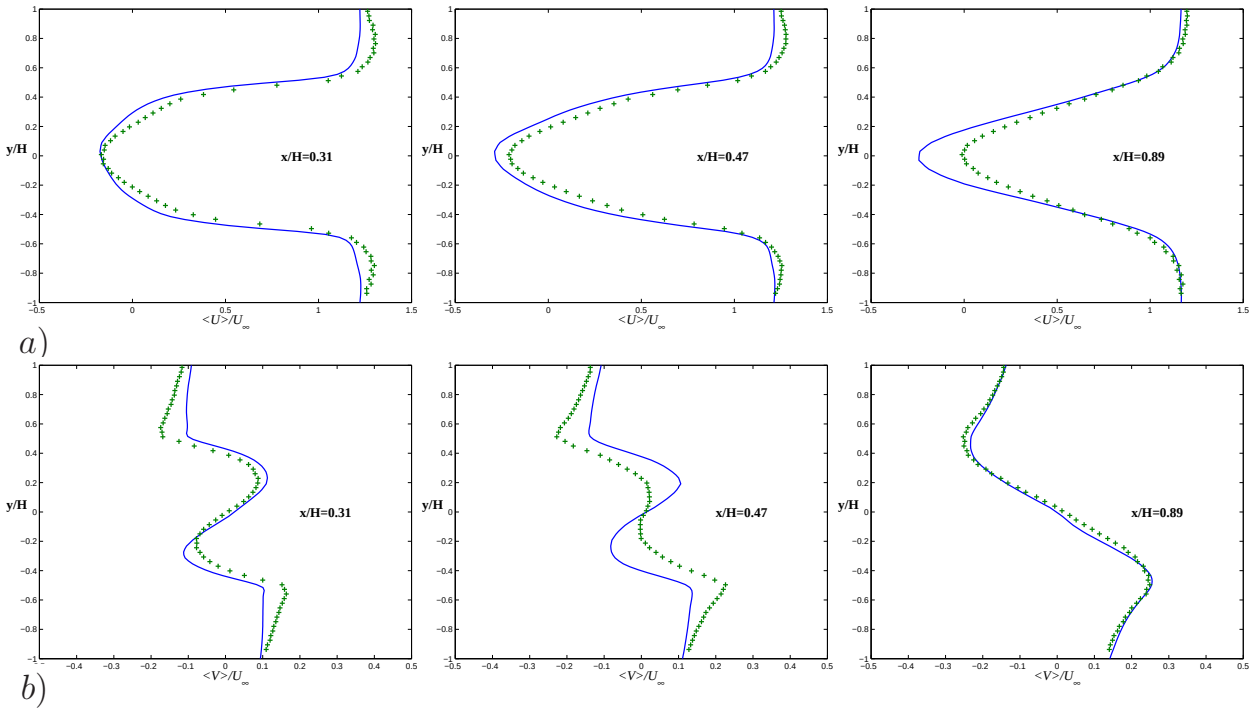

Figure 4.6: Controlled flow time-averaged velocity profiles at three downstream locations at $z = 0$. LES data (solid line); PIV data (symbols).

Comparison between LES and PIV time-averaged velocity profiles at three downstream locations is presented in Figs. 4.5 and 4.6. Results shows good agreement for both the natural and controlled flow. However, when compared with the natural case, larger differences in the controlled case results are visible both in the drag force values and the time-averaged velocity profiles. As we referred in section 3.1., a geometric simplification was introduced in the model's section. This fact can explain the greater deviations encountered between the LES and the experimental controlled flow results, which are observed in Table 4.2 and Fig. 4.6.

4.3 Exploring the flow

Visualization techniques based on critical-point theory and concepts [29], [30] are employed to explore the instantaneous and time-averaged flows at this Reynolds number. In contrast with the flow at low Reynolds number, described in *chapter 3*, the time-averaged natural flow at $Re_h = 2 \times 10^4$ presents one main separation and attachment regions, revealed in Figure 4.7. Measured relatively to the transition tape and at the symmetry plane, the separation and reattachment lengths are, respectively, $X_s = 0.343H$ and $X_a = 0.596H$. The trace lines pattern associated with these two main flow regions that is shown in Figure 4.7 *a*) and *b*) illustrates the two-dimensional nature of the flow at this Reynolds number. This visualization confirms what was directly deduced in *section 3.2* from the time-averaged pressure distribution along the spanwise direction of the body, in the near-wake region. Therefore, this means the wind tunnel walls play no significant role in the main time-averaged flow features. Figure 4.7 *c*) displays a detailed look into the flow pattern around one of the circular rods, used to mount the experimental model in the wind tunnel. From the winding shape of the separation and attachment curves, it can be concluded that further averaging time is needed to attain a statistical perfect time-averaged flow.

Examination of the separation bubble existing in the wake region is performed for the time-averaged natural flow in Fig. 4.8; and comparison with the time-averaged controlled case can be retrieved from Fig. 4.9. Both regions are projected into the symmetry plane, $z = 0$. The base flow consists of two large vortices, an upper clockwise rotating vortex and a lower counter-clockwise rotating vortex, originating, respectively, in the foci N_1 and N_2. N_1 is located at $\approx (0.498H, 0.215H, 0)$; and N_2 at $\approx (0.495H, -0.227H, 0)$. Two thin vortices are formed at the upper and lower edges of the rear face of the body, corresponding, respectively, to the foci N_3 and N_4. The time-averaged separation bubble length is $X_n = 0.965H$.

Similar analysis can be performed for the controlled flow case, from Fig. 4.9. And three major conclusions are attained. Firstly, the primary vortices F_1 and F_2 are located, respectively, at $\approx (0.599H, 0.227H, 0)$ and $\approx (0.619H, -0.246H, 0)$; from its x coordinate value, we can thus observe that the foci origin is displaced downstream in the controlled flow. Secondly, the separation bubble length is $X_c = 1.15H$; this represents an increase in the bubble length of $\approx 19.2\%$, relatively to the time-averaged natural flow case. Thirdly, the upper and lower-edge thin vortices are reduced in the controlled flow; this can be concluded from the relative size of the coherent structures F_3 and F_4, observed in Fig. 4.9.

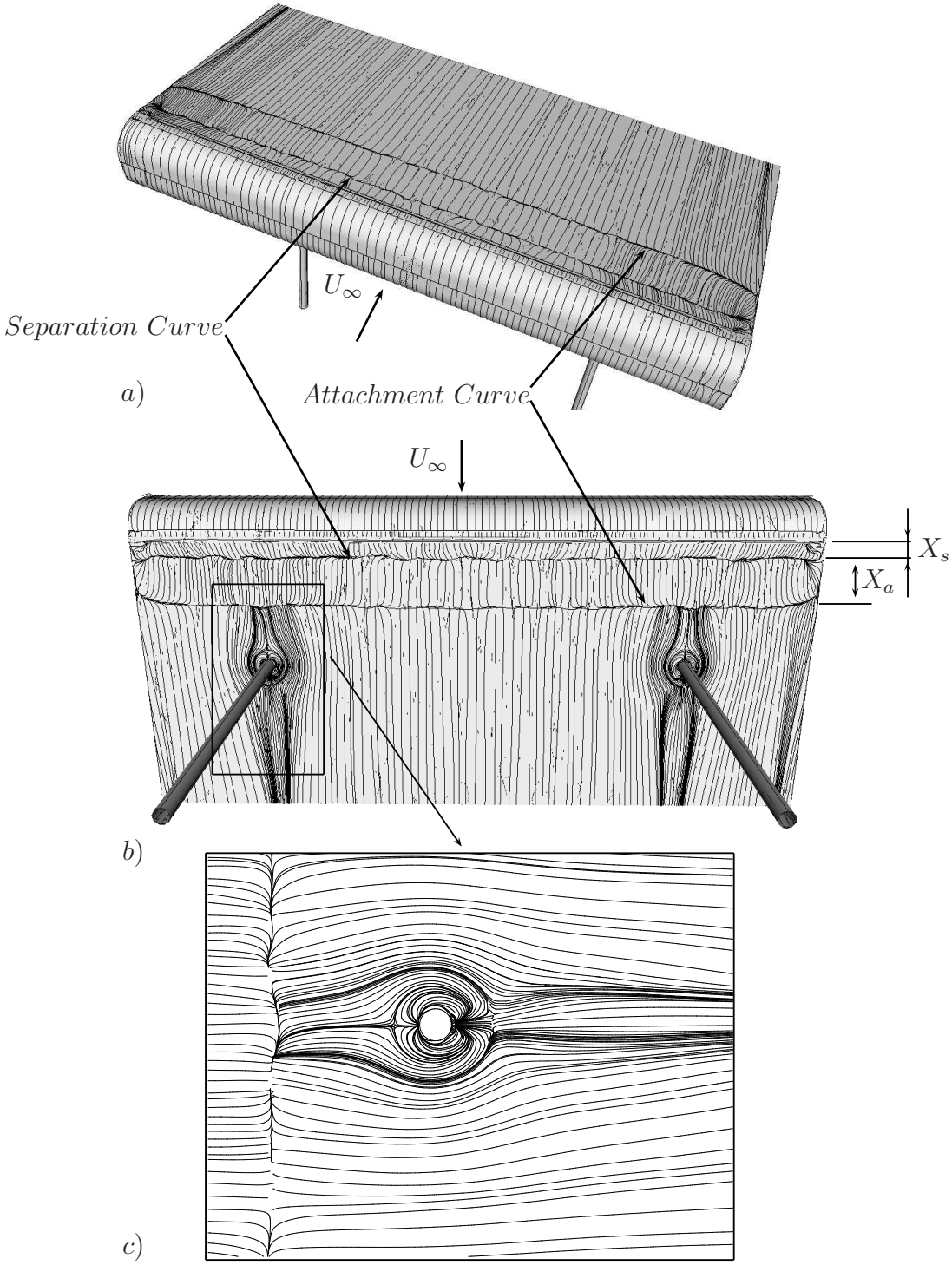

Figure 4.7: Natural flow time-averaged trace lines on the surface of the body, showing the separation and attachment curves. a) Perspective view of the frontal and top surfaces. b) Perspective view of the frontal and bottom surfaces. c) Zoom of b), showing the flow pattern around the wind tunnel mounting rod.

These informations and conclusions lead to the construction of a physical picture unveiling the effects of harmonic actuation in the bluff body wake. Considering the effects on the *mean flow statistics*, the actuation produces simultaneously an elongation in the separation bubble and a reduction in the upper and lower-edge thin vortices. The change in the bubble shape and location of the main turbulent coherent structures contributes to the decrease in turbulence intensity in the near wake region. This observation is supported by the comparison between the LES time-averaged velocity profiles for the base and the controlled case, for example, at $x/H = 0.5$ and $x/H = 0.47$ (Figs. 4.5 and 4.6). The physical process is mainly visible in the time-averaged transverse velocity component, $\overline{V}/U_\infty$. A lower turbulence intensity in the time-averaged controlled flow also indicates a lower vorticity intensity in the near-wake region, thus contributing to pressure recovery.

However, following Krajnović, S. in [34], a pertinent question is the real physical meaningfulness of the informations retrieved from the mean flow statistics. The flow around a bluff body is governed by the instantaneous turbulent coherent structures and it is, therefore, highly time-dependent. The controlled flow around the present model is particularly interesting in this sense, since there seems to exist a periodicity in the flow's features (supported by the periodicity in the drag force signal). It is thus logic attempting to understand the flow's evolution throughout one period of the drag force signal. Figures 4.10 to 4.13 represent the previous idea; the analysis of the instantaneous flow is

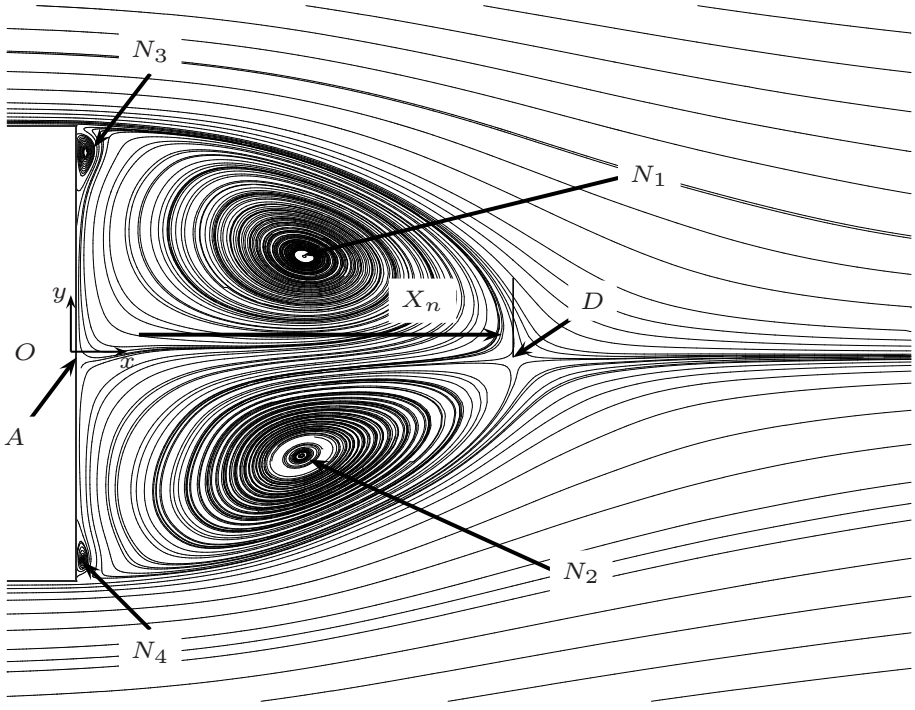

Figure 4.8: Natural flow time-averaged streamlines projected into the symmetry plane $z = 0$ of the vehicle model. View of the wake region. N_1 and N_2 are foci corresponding, respectively, to the upper (clockwise) and lower (counter-clockwise) vortices and D is the saddle point. N_3 is associated with the upper-edge thin vortex (counter-clockwise). N_4 is related with the lower-edge thin vortex (clockwise). The stagnation point is located at A.

performed using streamlines visualization, pressure distribution in the near-wake region and one vorticity isosurface, coloured with velocity magnitude. It should be also referred that the dashed curve in the drag force signal is associated with a function with the same frequency as the actuation frequency, w_A.

Starting the flow analysis at $t^* = 128.9$, a transition instant between suction and blowing, two primary turbulent structures C_1 and C_2 are found in Fig 4.10 *a*); at the upper edge of the rear face, a coherent structures group, C_3, is visualized in the same illustration. The corresponding pressure coefficient at $z = 0$ is observed to be quite uniform in Fig 4.10 *b*), with its minimum value at $x/H = 0.014$ close to the upper edge of the stern. The vorticity isosurface $\omega = 420$ presents a low intensity in center region of the near-wake, as it is shown in Fig 4.10 *c*). Figure 4.11 presents the same physical data for an instant close do peak blowing and, consequently, to maximum drag force. At this instant, two synchronized turbulent coherent structures are visualized with increased definition, C_5 and C_6; the pressure coefficient profile at $x/H = 0.014$ drops. At Fig. 4.11 *c*), the synchronized *roll-up* of the vorticity isosurface $\omega = 420$ is observed, from the upper and lower shear layers. A transition instant, this time between blowing and suction, follows from Fig. 4.12. Two conclusions are clear from Fig. 4.12 *a*): firstly, the two primary coherent structures *remain* defined and *synchronized* (C_7 and C_8); secondly, the separation bubble elongates downstream, which is visualized from the x coordinate position of the saddle point, H.

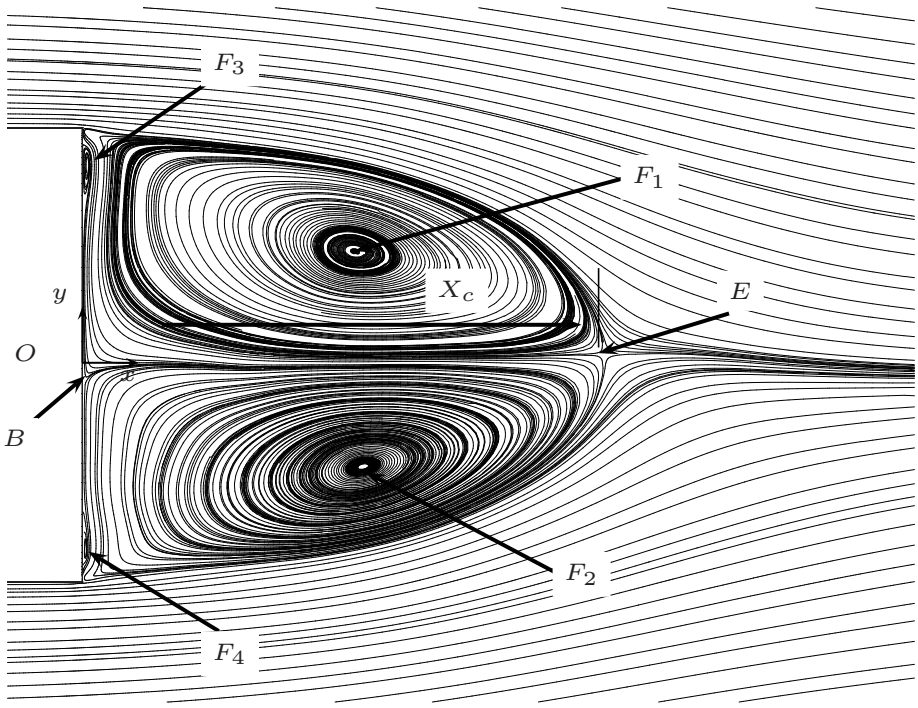

Figure 4.9: Controlled flow time-averaged streamlines projected into the symmetry plane $z = 0$ of the vehicle model. View of the wake region. F_1 and F_2 are foci associated with the upper (clockwise) and lower (counter-clockwise) vortices and E is the saddle point. F_3 and F_4 are foci corresponding, respectively, to the upper-edge (counter-clockwise) and lower-edge (clockwise) thin vortices. B is the stagnation point in the rear face of the model.

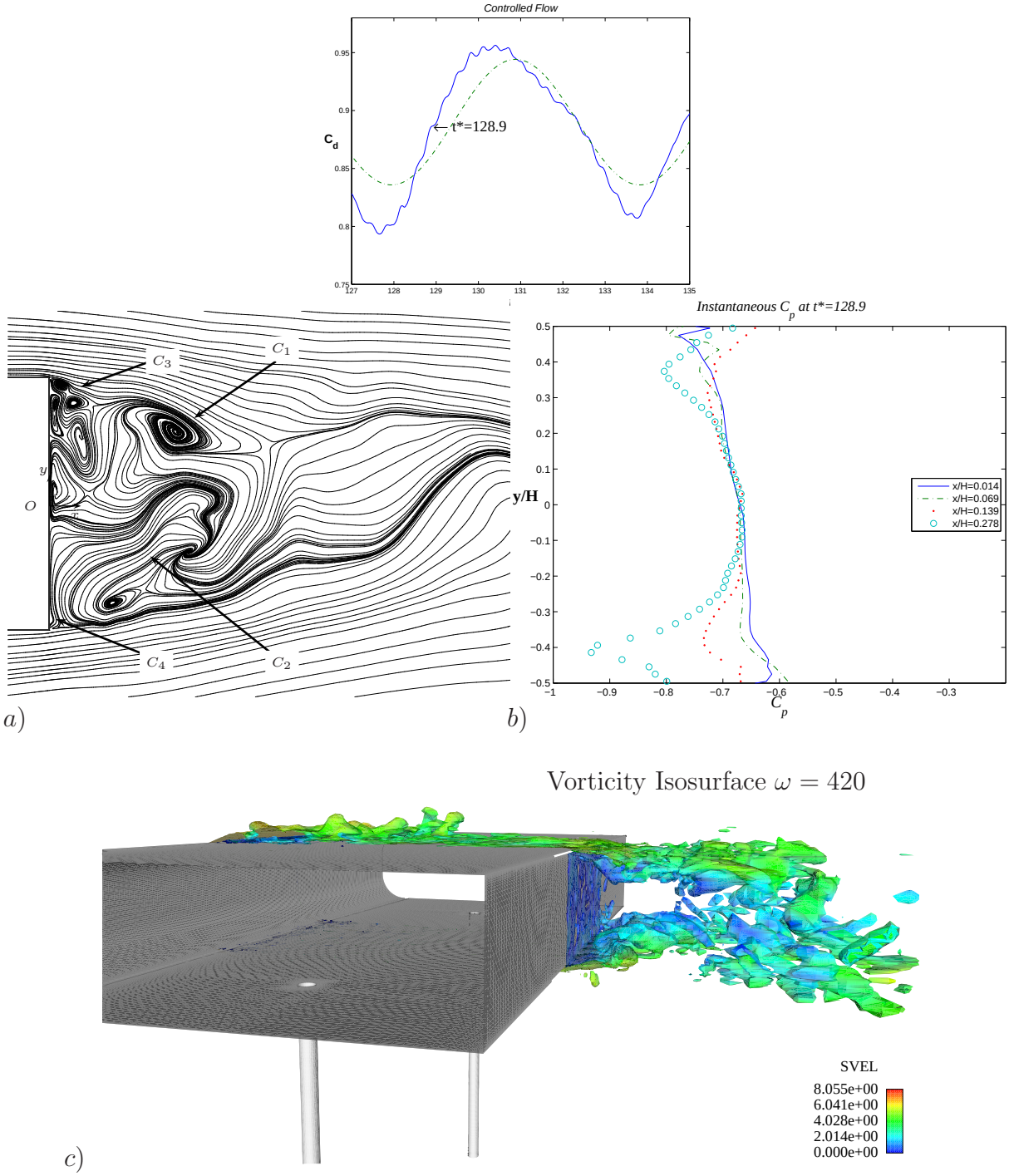

Figure 4.10: Exploring the instantaneous controlled flow at time $t^* = 128.9$, view of the wake region at $z = 0$. a) Instantaneous streamlines projected into the symmetry plane. b) Instantaneous pressure coefficient along the model's height, at four x/H locations. c) Perspective view of the vorticity isosurface $\omega = 420$ coloured with velocity magnitude.

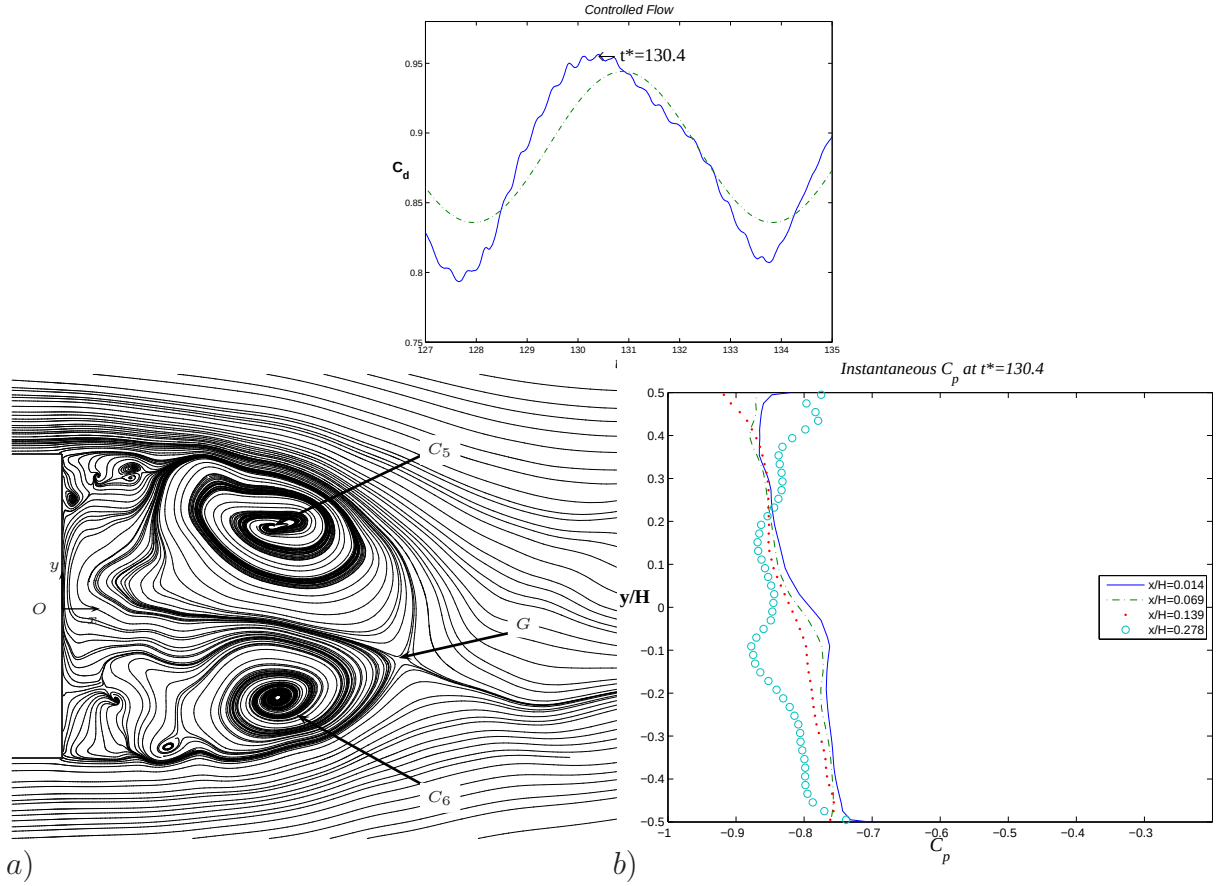

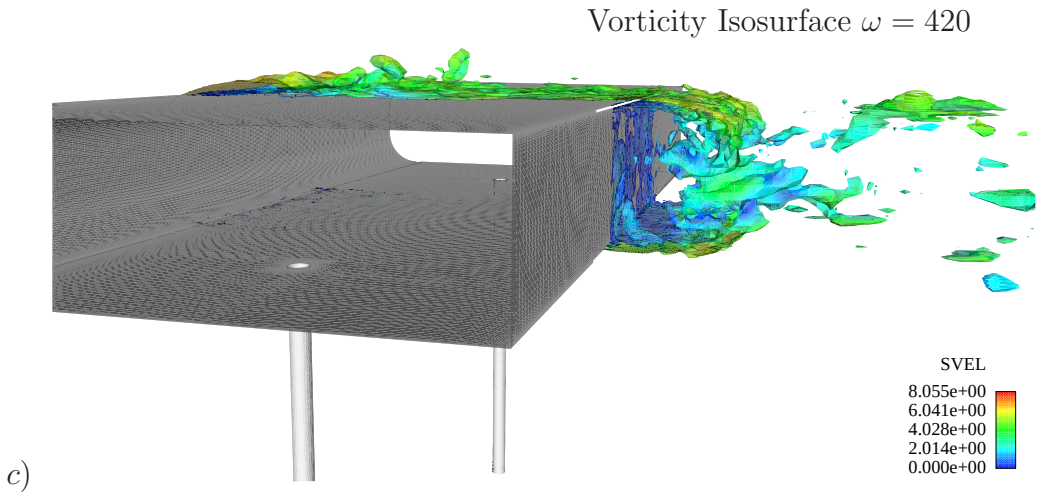

Figure 4.11: Exploring the instantaneous controlled flow at time $t^* = 130.4$, view of the wake region at $z = 0$. a) Instantaneous streamlines projected into the symmetry plane. b) Instantaneous pressure coefficient along the model's height, at four x/H locations. c) Perspective view of the vorticity isosurface $\omega = 420$ coloured with velocity magnitude.

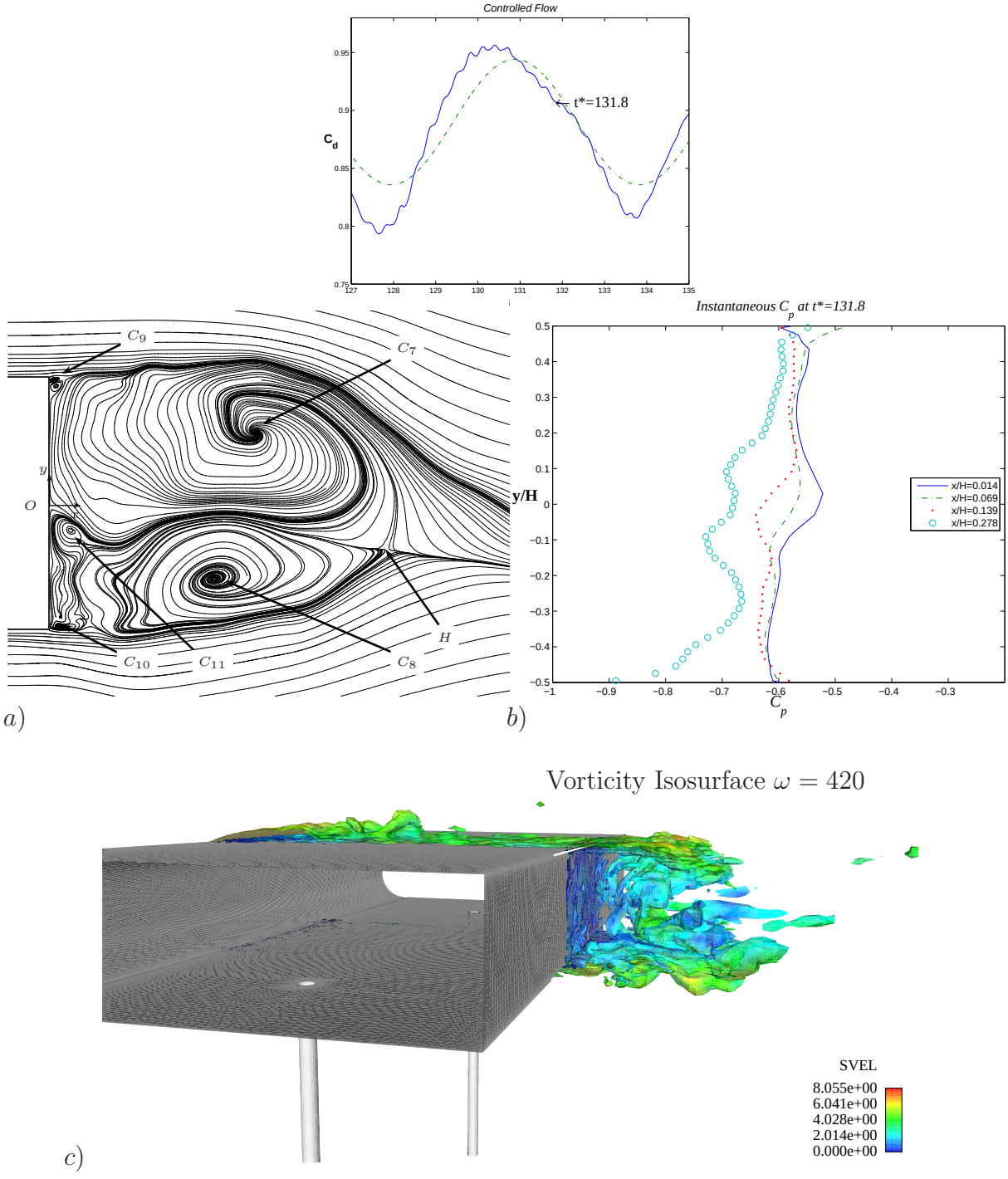

Figure 4.12: Exploring the instantaneous controlled flow at time $t^* = 131.8$, view of the wake region at $z = 0$. a) Instantaneous streamlines projected into the symmetry plane. b) Instantaneous pressure coefficient along the model's height, at four x/H locations. c) Perspective view of the vorticity isosurface $\omega = 420$ coloured with velocity magnitude.

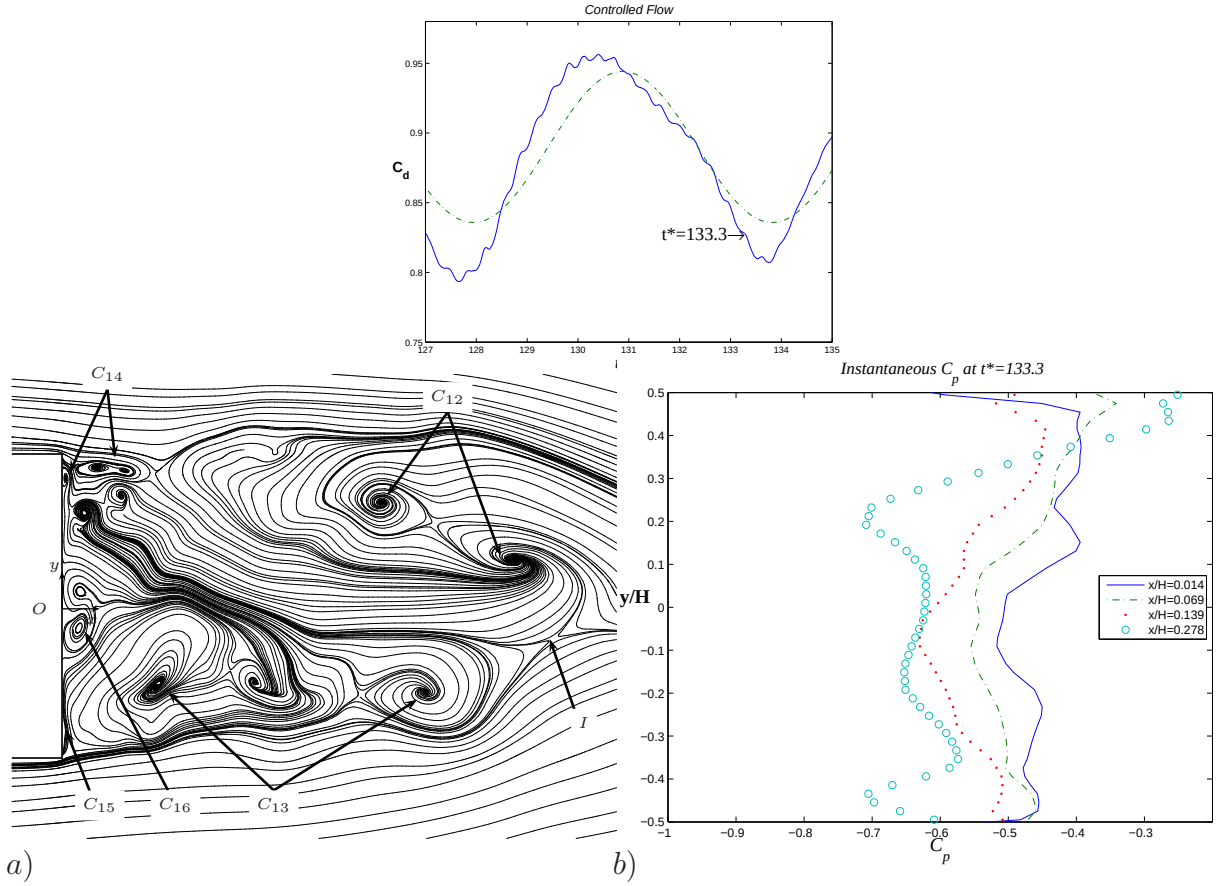

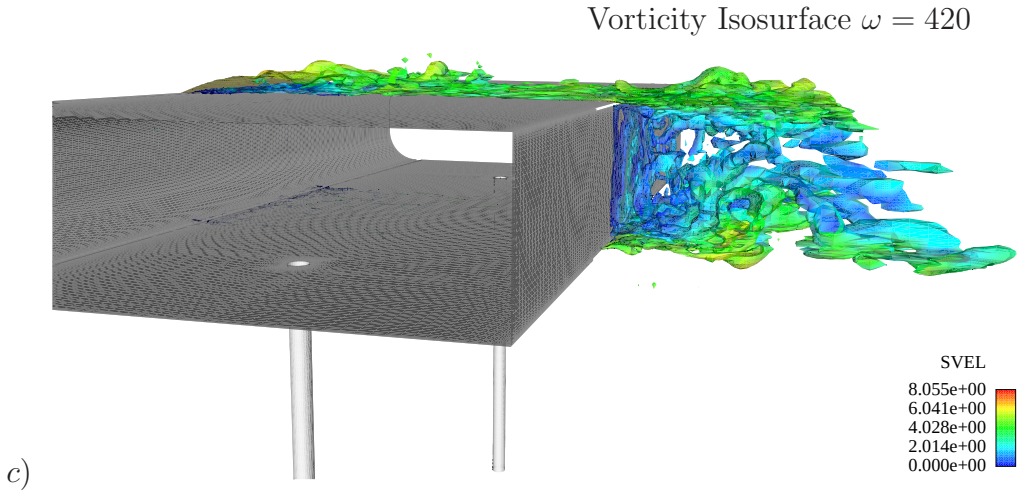

Figure 4.13: Exploring the instantaneous controlled flow at time $t^* = 133.3$, view of the wake region at $z = 0$. a) Instantaneous streamlines projected into the symmetry plane. b) Instantaneous pressure coefficient along the model's height, at four x/H locations. c) Perspective view of the vorticity isosurface $\omega = 420$ coloured with velocity magnitude.

Consequently, the pressure at $x/H = 0.014$ is observed to restart a recovery trend. A common feature with the time-averaged pressure coefficient profile at $x/H = 0.014$ is its uniformity, found along the instantaneous profiles analyzed previously. Figure 4.12 *b*) also retains this feature. Finally, moving on to the instant $t^* = 133.3$, we can understand the flow's attributes close to peak suction. It is interesting to observe in Fig 4.13 *a*) how the turbulent structures respond to the actuation at this time. Each of the two main coherent structures found in previous instants seems to break up into a couple of smaller structures, pointed by C_{12} and C_{13}. The saddle point I is located further downstream. Near the rear face, a group of turbulent structures, C_{14}, C_{15} and C_{16}, is distributed from the upper to the lower edge of the body. The actuation at this time seems, therefore, to promote a certain degree of "homogeneity" in the bluff body wake. The pressure recovery attains its maximum at this time, as shown in Fig. 4.13 *b*). The actuation hence dominates the flow and promotes a decrease in wake instabilities. Figure 4.13 *c*) illustrates how the phenomena is reflected in the vorticity isosurface $\omega = 420$. The roll-up phenomena identified at $t^* = 130.4$ has disappeared from the central region of the near-wake, which is coherent with the streamlines visualization; and the vorticity density in the central region also seems to follow a decreasing trend, resembling what is visualized at $t^* = 128.9$ in Fig. 4.10 *c*).

The time-averaged and instantaneous controlled flow around the vehicle model has, therefore, been explored. The main findings about the physical nature of the flow can be summarized in the following ideas:

1. Harmonic actuation in the bluff body wake successfully suppresses the total wake instability, which is the physical phenomena governing the natural flow case.

2. The suppression of this flow mechanism is achieved through the synchronized formation of the main turbulent coherent structures in the bluff body wake, which is observed in the instantaneous controlled flow.

3. Together with the synchronized turbulent structures formation, the actuation promotes the displacement of these coherent structures further downstream in the wake region, when compared with the base flow case. This mechanism is present both in the time-averaged and in the instantaneous flow and produces a significant change in the shape of the separation bubble.

4. The elongation of the separation region is connected with the formation of a lower turbulence intensity zone in the near-wake region. A pressure recovery in this region is thus induced by these physical mechanisms.

5. Ultimately, pressure recovery in the near-wake region induces a drag force reduction.

Chapter 5

Conclusions and suggestions for future work

The present investigation has aspired and achieved three primary goals. Firstly, the main issues in CFD for active flow control implementation have been overcome; it has been shown that a simple analytic function implemented as a traditional boundary condition, with adequate temporal and spatial resolutions in the actuator region, can be used to model the actuator and the actuator-induced flow. Secondly, the ability to actively control the flow around a two-dimensional bluff body has been proved; this has been recognized from a drag force signal that responds with the same frequency as the actuation frequency. Thirdly, the understanding about the physical mechanisms responsible for drag force reduction has been increased through the exploration of the detailed and accurate flow information given by LES.

The main finding is, therefore, undoubtably associated with drag force reduction. The potential for beneficial performance increase in vehicle aerodynamics from harmonic actuation in the vehicle wake region has been confirmed by the 10% drag reduction attained from the flow at $Re_h = 2 \times 10^4$. Results validation and comparison with experimental data available also sustain this conclusion. The physical nature of the controlled flow is significantly different from the base flow. It has been observed that the actuation in the bluff body wake promotes the suppression of the alternating sequence of strong instabilities, originating from the upper and lower shear layers, which govern the natural flow. This is achieved through synchronized vortex formation in the wake region. Together with the formation of synchronized turbulent coherent structures, the actuation displaces these structures further downstream, thus "delaying" the formation of the vortex shedding phenomena. A significant change in the separation bubble shape has been observed both in the instantaneous and time-averaged flow, due to the previous mechanism. The elongation of the separation region is connected with the existence of a lower turbulence intensity zone in the near-wake region. This triggers a pressure recovery in the near-wake and, consequently, a drag force reduction.

Limitations in the application of these results to a *real* case are, however, encountered. These limitations are concerned with the bidimensional nature of the vehicle model and its position in the wind tunnel, which does not represent an applicable case. The flow around a three-dimensional bluff body is strongly influenced by longitudinal vortices orig-

inating both from the upper and lower edges and the lateral edges of the rear face. It is thus not expectable that the control strategy used here will achieve a promising drag force reduction. At least, not without significant changes. This is, therefore, a research subject for future work. The application of harmonic actuation in time to the flow around other types of bluff bodies, such as train or car models, is also included in the topic for future work. The advances in computational power and control theory will support the development of active flow control research within the next decade. And, hopefully, the understanding gained from research in this field will be able to bring active flow control systems into the transportation industry.

Bibliography

[1] M. Gad-el Hak, A. Pollard, and J.P. editors Bonnet. *Flow Control: Fundamentals and Practices*. Springer, 1998.

[2] S. Collins, R.D. Joslin, A. Seifert, and V. Theofilis. Issues in active flow control:theory,control,simulation, and experiment. *Progress in Aerospace Sciences*, 40:237–289, 2004.

[3] M. Gad-el Hak, A. Pollard, and J.P. editors Bonnet. *Flow Control: Fundamentals and Practices*. Springer, 1998.

[4] A.J. Stuart and W.C. Reynolds. Active control of streamwise vortices and streaks in boundary layers. *Journal of Fluid Mechanics*, 360:179–211, 1998.

[5] R. Rathnasingham and K.S. Breuer. Active control of turbulent boundary layers. *Journal of Fluid Mechanics*, 495:209–233, 2003.

[6] L. Yong and M. Gaster. Active control of boundary-layer instabilities. *Journal of Fluid Mechanics*, 550:185–205, 2006.

[7] H. Fu and D. Rockwell. Shallow flow past a cylinder: control of the near wake. *Journal of Fluid Mechanics*, 539:1–24, 2005.

[8] E.A Gillies. Low-dimensional control of the cylinder wake. *Journal of Fluid Mechanics*, 371:157–178, 1998.

[9] J. Gerhard, M. Pastoor, R. King, B.R. Noack, A. Dillmann, M. Morzyński, and G. Tadmor. Model-based control of vortex shedding using low-dimensional Galerkin models. In *33rd AIAA Fluids Conference and Exhibit*, Orlando, Florida, U.S.A., June 23–26, 2003, 2003. Paper 2003-4262.

[10] J.F. Donovan, L.D. Kral, and A.W. Cary. Active flow control applied to an airfoil. *AIAA Paper No 98-0210, 36th AIAA Aerospace Sciences Meeting, Reno*, 1998.

[11] J.A. Ekaterinaris. Prediction of active flow control performance on airfoils and wings. *Aerospace Science and Technology*, 8:401–410, 2004.

[12] R. Duvigneau and M. Visonneau. Optimization of a synthetic jet actuator for aerodynamic stall control. *Computers & Fluids*, 35:624–638, 2006.

[13] M. Shatz, F. Thiele, R. Petz, and W. Nitshe. Separation control by periodic excitation and its application to a high lift configuration. In *AIAA Paper 2004-2507*. 2nd AIAA Flow Control Conference, 28 June - 1 July 2004, Doubletree Beach and Columbia River, Portland, Oregon, AIAA, 2004.

[14] P. Kjellgren, N. Anderberg, and I. Wygnaski. Download alleviation by periodic excitation on a typical tilt-rotor configuration - computation and experiment. *AIAA Paper No 2000-2697, Fluids 2000, 19-22 June 200, Denver*, 2000.

[15] P. Spalart, L. Hedges, M. Shur, and A. Travin. Simulation of active flow control on a stalled airfoil. *Flow,Turbulence and Combustion*, 71:361–373, 2003.

[16] D. You and P. Moin. Large-eddy simulation of flow separation over an airfoil with synthetic jet control. *APS Meeting Abstracts*, 2006.

[17] US Department of Transportation Research and Inovative Technology Administration (RITA).

[18] L. Henning, M. Pastoor, R. King, B.R. Noack, and G. Tadmor. Feedback control applied to the bluff body wake. In editor King, R., editor, *Notes on Numerical Fluid Mechanics and Multidisciplinary Design (NNFM)*, Berlin,Germany, 2007. 1st Active Flow Control Conference (AFC 2006), Springer,2007.

[19] J. Kim, S. Hahn, J. Kim, D. Lee, J. Choi, W. Jeon, and H. Choi. Active control of turbulent flow over model vehicle for drag reduction. *Journal of Turbulence*, 5,019, 2004.

[20] E. Brunn, A.and Wassen, D. Sperber, W. Nitsche, and F. Thiele. Active drag control for a generic car model. In *Proceedings of the Conference on Active Flow Control 2006, Notes on Numerical Fluid Mechanics and Multidisciplinary Design*, volume 95, pages 247–259. Springer Verlag, 2007.

[21] A.N. Kolmogorov. Local structure of turbulence in an incompressible fluid for very large reynolds number. *Comptes rendus (Doklady) de l'Academie des Sciences de l'U.R.S.S.*, 31:301–305, 1941.

[22] S. Gamard and W.K. George. Reynolds number dependence of energy spectra in the overlap region of isotropic turbulence. *Flow, Turbulence and Combustion*, 63:443–477, 2000.

[23] Pierre Sagaut. *Large eddy simulation for incompressible flows*. Springer, 2nd edition, 2002.

[24] Siniša Krajnović. *Large-eddy simulations for computing the flow around vehicles*. Phd thesis, Department of Thermo and Fluid Dynamics, Chalmers University of Technology, SE-412 96, Gothenburg, Sweden, ISBN 91-7291-188-3, 2002.

[25] S. Krajnović and L. Davidson. Large-eddy simulation of the flow around a ground vehicle body. *SAE Paper*, pages 2001–01–0702, 2001.

[26] S. Krajnović and L. Davidson. Large-eddy simulations of the flow around a simplified bus. In *3rd AFOSR International Conference on DNS and LES*, 2001.

[27] J. Chasnov and U. Piomelli. Large-eddy simulations: theory and applications, 1996.

[28] Hassan Nasr Hemida. *Large-eddy simulation of the flow around simplified high-speed trains under side wind conditions*. Licentiate thesis, Department of Thermo and Fluid Dynamics, Chalmers University of Technology, SE-412 96, Gothenburg, Sweden, ISSN 1652-8565, 2006.

[29] A. E. Perry and M. S. Chong. A description of eddying motions and flow patterns using critical-point concepts. *Annual Review of Fluid Mechanics*, 19:125–155, 1987.

[30] J. Jeong and F. Hussain. On the identification of a vortex. *Journal of Fluid Mechanics*, 285:69–94, 1995.

[31] Lars Henning. Private communication. 2007.

[32] Pastoor, M. and Henning, L. and Noack, B. R. and King, R. and Tadmor, G. Feedback layer control for bluff body drag reduction. *Journal of Fluid Mechanics*, 2007. Submitted for publication.

[33] Pastoor, M. and Henning, L. and Noack, B. R. and King, R. and Tadmor, G. PIV data. Private communication, 2007.

[34] S. Krajnović and L. Davidson. Flow around a simplified car, part 2: Understanding the flow. *Journal of Fluids Engineering*, 127.